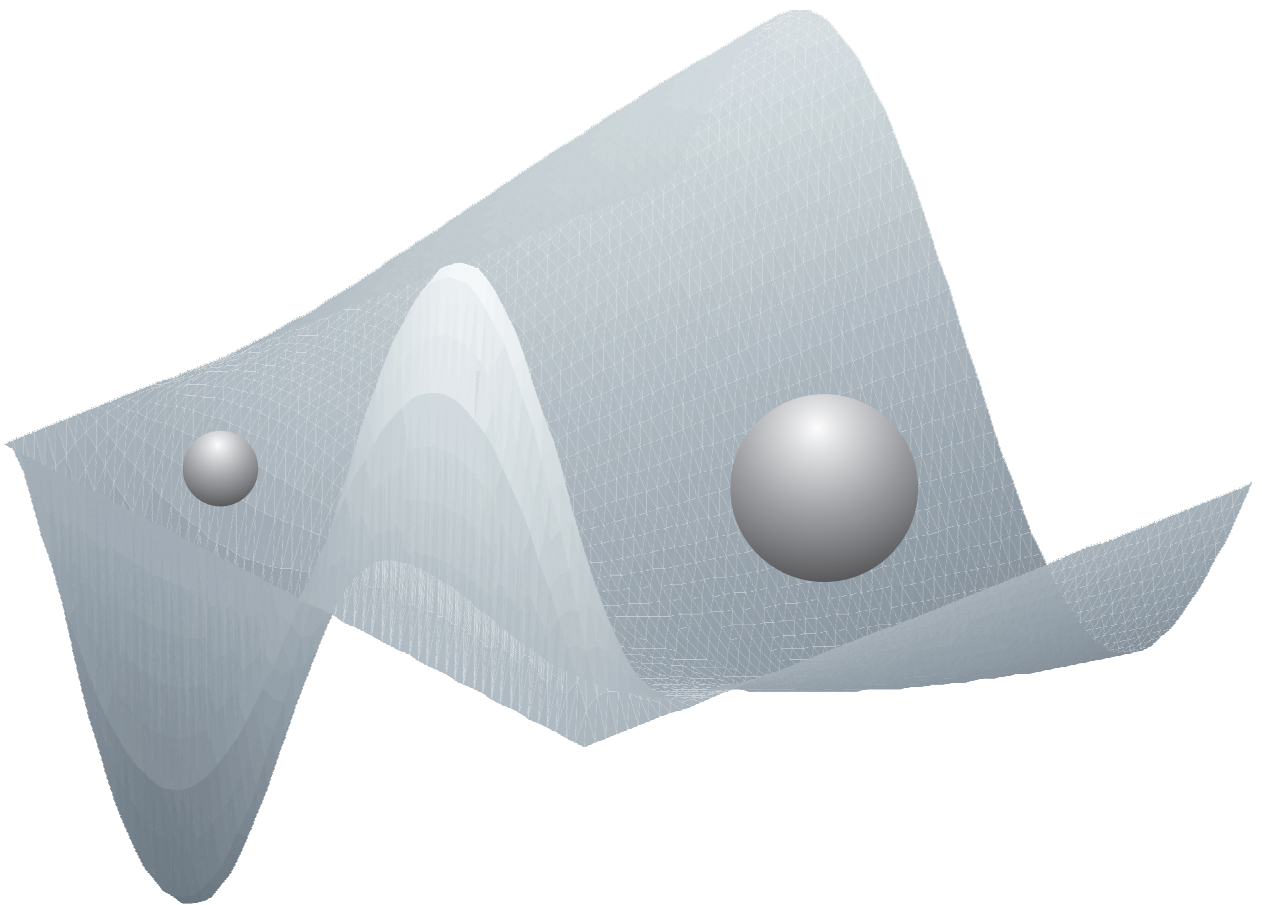


Nanomechanical Sensing in Liquid



Marko Dorrestijn

Nanomechanical Sensing in Liquid

Inauguraldissertation

zur

Erlangung der Würde eines Doktors der Philosophie
vorgelegt der
Philosophisch-Naturwissenschaftlichen Fakultät
der Universität Basel

von

MARKO DORRESTIJN

aus den Niederlanden

Rüschlikon, 2006

Genehmigt von der Philosophisch-Naturwissenschaftlichen Fakultät

auf Antrag von

Prof. Dr. E. Meyer

Prof. Dr. Ch. Gerber

Basel, den 24. Januar 2006

Dekan
Prof. Dr. Hans-Jakob Wirz

The cover shows the stream function of boundary streaming near a nanomechanical oscillator in liquid. The small and large particles follow different flow directions.

The research reported in this dissertation was financially supported by the National Center of Competence in Research on Nanoscale Science (NCCR Nanoscale Science), the Technology-Oriented Program TOP NANO 21, and the Cleven-Becker-Stiftung.

Preface

In the 1990's, revolutions in two fields of research had generated a powerful new synergy, popularly called "NanoBio". The revolutions were Nanotechnology in materials science and a novel toolbox in biotechnology. The term Nanotechnology described the newly acquired ability to build structured materials "bottom-up". Atoms could be seen and manipulated by the Scanning Tunneling Microscope (IBM, 1982 & 1989), molecules could "walk" (IBM, 1999), and carbon nanotubes were found to be stronger than steel and to have interesting electronic properties as well.

In biotechnology, a similar bottom-up approach had been developed in the form of three novel tools. The first was recombinant DNA technology (Cohen and Boyer, 1973), which was later used to create micro-organisms that produce human insulin (Genentech, 1982). The second tool was the hybridoma technology (MRC Cambridge, UK, 1975), with which specific antibodies could be generated in vitro, e.g. for pregnancy tests. The third important instrument was the Polymerase Chain Reaction (Cetus Corporation, 1980's). It provided essentially unlimited quantities of the genetic material molecular biologists required for their work.

It was in this interesting time that I decided to study "NanoBio". The only problem was, no university offered this program. My solution was to study Applied Physics in Delft, and simultaneously take Molecular Biology courses in Leiden. When I presented my Bachelor's work at Nanotech 2000 in Switzerland, I came into contact with the Cantilever Sensor group at the IBM Zurich Research Laboratory. I found it to be an ultimately NanoBio project, and I was excited that Prof. Christoph Gerber, Master of the AFM, and Prof. Ernst Meyer, head of the UHV Force Microscopy group of the University of Basel, offered me the Ph.D. position. It was the start of a very rewarding collaboration. Christoph and Ernst left me an enormous amount of freedom in the project while giving much constructive feedback. Thank you, Ernst, for giving me the opportunity to do a Ph.D. with the University of Basel, and for being my "Doktorvater". Whenever I came to Basel, you would take the time to analysis of my results; it was instructive to see how you would boil down the fluid dynamics to a simple equation, reach for your calculator, and ballpark the bead velocities. Prof. Gerber supervised me to most. The first thing I learned from you, Christoph, was to take responsibility for my own results. The second thing was "schnäll bastle"; your anecdotes on solder- and tape-covered SPM prototypes taught me that your secret was actually a slogan by Nike: 'Just do it'. I would like to thank Prof. Güntherodt, president of the NCCR Nanoscale Science, for making this opportunity available to me. I also profited enormously from seven NCCR-sponsored conferences. Furthermore, I acknowledge the financial support of the technology-oriented program TopNano21.

Many thanks go to my colleagues as well. First of all to Dr. Alexander Bietsch and Dr. Hans Peter Lang. Hans Peter, I appreciate your support in teaching me the ins and outs of the lab equipment, how to build liquid cells and where to find gadgets in the L207 haystack. Thanks also for the many fruitful discussions. Alex, I enjoyed our collaboration and it was motivating for me to

learn your key success factor: understanding the underlying physics of every intermediate result.¹ In Basel, my closest collaborators were Dr. Viola Barwich and Murali Ghatkesar, with whom it was exciting to add pieces to the dynamic-mode-in-liquid puzzle. To my other colleagues in Basel I owe much as well: Dr. Rachel McKendry, Dr. Thomas Braun, Dr. François Huber, Dr. Natalija Backmann, Dr. Natalia Nugaeva, Avigail Abuhatsira, Dr. Wilfried Grange, Marc Karle, and Kate Rakhmatullina, thanks for the great collaboration and for your friendship. A special thanks goes to Jean-Pierre Ramseyer, for his unconditional technical support, and to Dr. Martin Hegner, head of the Biophysics group, for many fruitful discussions and for being able to make a joke when we needed one.

At the IBM Zurich Research Laboratory, the facilities were fantastic. First of all, the electronics workshop and the model shop were second to none. There was also a superb metal evaporator, a high-resolution SEM, and a wafer fab. I am grateful to Ute Drechsler and Dr. Michel Despont for fabricating cantilever arrays of such high quality. In Site Operations, I further thank Publications for revamping our publications, the library for delivering even the rarest books,² and Information Services for always fixing my PC within minutes.³ The Hobby Club was a key driver for the pleasant collaboration in IBM.⁴ I thank Dr. Paul Seidler, head of the Science and Technology department, and my manager Dr. Rolf Allenspach, head of the Physics of Nanoscale Systems group, for giving me the opportunity to be part of this stimulating environment. Rolf, I benefitted much from your coaching, and I appreciated the physics you taught me over lunch in the form of anecdotes and even trivia games.⁵

Our collaborators at the ETH Zurich and at Purdue University provided valuable complements to our experimental results. At Purdue, Prof. Arvind Raman and Dr. Tolga Açıkalın contributed a superb model for acoustic streaming; at the ETH, Dr. Jens Walther and Prof. Petros Koumoutsakos provided us with excellent simulations of our oscillating cantilevers in water.

I thank my parents for backing my choice to embark on a study in Applied Physics, and for their support. I am grateful to my friends, who made sure that I got plenty of exercise on the gravel, in the snow, and on the fairway. Also Maya and Rolf Frischke, I much appreciate your many efforts to Swissify me with cheese, Swiss wine, and jokes about people from Bern. Finally, I thank my fiancée Laura for simply being the wonderful person she is.

Marko Dorrestijn,
Rüschlikon, January 2006.

¹In fact, Alex' method seemed to follow what was written in 1932 on the stairs of the IBM Schoolhouse in Endicott, NY: Think, Observe, Discuss, Listen, Read.

²And Swiss chocolates.

³The TRA syndrome, technology-related anger, was unheard of in the lab.

⁴In general, personal interaction was strongly promoted at IBM. Executives at the headquarters in Armonk once asked in bewilderment what it was about the Zurich lab that all four IBM Nobel laureates came from there. The answer they got was: 'The cafeteria.'

⁵For example 'Which of the formulas on your T-shirt describes Faraday's Law,' and 'Which Dutchman invented superconductivity and when? Hint: It was 50 years before Bill Haley.'

Contents

Preface	i
Abstract	iv
1 Introduction	1
2 A novel displacement sensor based on a squeezable molecular multilayer	3
2.1 Tunneling readout using molecular bilayers	3
2.2 Capacitive readout using molecular multilayers	8
3 Nanomechanical resonators generating Chladni figures and acoustic streaming	16
3.1 A brief history of Chladni figures and acoustics	16
3.2 Chladni figures in microfluidics	20
3.3 The physics of boundary streaming near an oscillating surface	32
4 Conclusions and Outlook	41
Bibliography	44
Curriculum Vitae	51

Abstract

This thesis describes advances in the field of nanomechanical sensors operating in liquid. Firstly, a novel method for measuring nanoscale displacements is presented. Secondly, microscale Chladni-figures are demonstrated on oscillating cantilevers by means of boundary streaming in the aqueous environment. Thirdly, the physics of boundary streaming is clarified for the first time. The three topics are summarized below.

A novel displacement sensor based on a squeezable molecular multilayer

A novel displacement sensor for nano- and micro-electromechanical devices (NEMS and MEMS) is introduced. The technique is based on a squeezable molecular multilayer, combined with electron tunneling or with capacitive readout. The main advantage is the predefined alignment of the electrodes, allowing miniaturization of traditional tunneling and capacitive sensors. Furthermore, the device can be operated in aqueous solutions. The multilayers consisted of stacked self-assembled monolayers (SAMs) of mercaptohexadecanoic acid. Capacitive measurements revealed the dielectric constant of the multilayers, which was $\epsilon_r = 1.5$. Squeezing of a bilayer lead to an exponential change in a tunnel current, resulting in nanometer displacement sensitivity.

Nanomechanical resonators generating Chladni figures and boundary streaming

Chladni figures based on nanomechanics in the microfluidic environment are presented. In contrast to the macroscopic observations in the gaseous environment, nanoparticles were found to move to the nodes, whereas micron-sized particles moved to the anti-nodes of the vibrating interface. This opens the door to size-based sorting of particles in microfluidic systems, and to highly parallel and controlled assembly of biosensors and nanoelectronic circuits.

The physics of boundary streaming

The physics of boundary streaming is revealed for the first time. This vortex flow phenomenon occurs near all oscillating surfaces in fluid media, therefore affecting operation of cantilever sensors and other nanomechanical devices with oscillating components. Here, a solution to the Navier-Stokes equation is obtained by using a series of physical analogies, giving full insight into the physics of boundary streaming.

Chapter 1

Introduction

The most widespread nanomechanical sensors are those based on the microcantilever. The first such sensor was the atomic force microscope (AFM), which was invented in 1986 by Binnig, Quate and Gerber [BQG86]. The cantilever was laser-cut from gold foil and had a diamond tip glued to its free end.¹ Deflection of the free end was measured by a tunnel current between the cantilever and a carefully aligned tip from a scanning tunneling microscope (STM). Two years later, atomic resolution was achieved by Heinzelmann and Meyer et al. [HMG88]. By replacing the tunneling readout by laser beam deflection [MA88], AFM could also be performed in the aqueous environment. The main advantage over imaging in air is the absence of a water film on the surface, increasing the resolution. Another improvement was the oscillating cantilever, which reduced the interaction forces with the surface. The AFM inspired many scientists, which led to the invention of a number of other types of scanning probe microscopes (SPMs), including the magnetic resonance force microscope (MRFM) [RYS92, RBM04], and the “chemical AFM” or time-of-flight scanning force microscope (TOF-SFM) [LWB04].²

But the most striking invention that followed the AFM was the “artificial nose”. In the years ’90–’91, the first discussions for the recently developed chemical AFM led to an interesting side-track. What if cantilevers were applied as bimetallic temperature sensors? It did not take the IBM scientists long to calculate the extreme sensitivity. This encouraged them to try and measure the heat from a chemical reaction at the cantilever surface. The calorimetric sensor was published in 1994 by Gimzewski, Gerber, Meyer, and Schlittler [GGM94]. It turned out that even the binding of molecules on its own produced enough mechanical stress to produce a detectable signal [BDL98]. This opened a door to cantilever-based biosensors in the fields of medicine and biology; it led to cantilever-based DNA hybridization assays [FBL00] and immunoassays [ASL03, BZH05].

Reference cantilevers are used to remove artifacts from the signal. However, this requires the signal transduction (the deflection to voltage conversion) to be equal for all cantilevers, which is experimentally challenging. At least, when static deflection is measured. When the cantilevers are oscillated, the problem is circumvented: only changes in the resonance frequency are used as a measure for binding mass. This recent development is called *dynamic mode* operation.

When nanomechanical devices oscillate in a medium, interesting fluid dynamics take place. Steady vortices are generated close to the oscillating surface, a phenomenon known as acoustic streaming. This streaming causes additional dissipation and mixing of the medium. Dissipation reduces the quality factor, which is a disadvantage for most sensors. The possibility of mixing,

¹Nowadays, most cantilevers are microfabricated from silicon, silicon nitride, or polymer.

²In the TOF-SFM, an AFM cantilever can pick up a molecule from the surface and accelerate it into a time-of-flight mass-spectrometer.

however, is an opportunity in microfluidic sensors. The reason is that at the microscale, mixing is usually limited by diffusion. The role of acoustic streaming in SPM imaging and cantilever-based sensors has been left largely (if not entirely) undiscussed. It is one of the purposes of this thesis to initiate activity on this subject.

The goal of this Ph.D. research was to further the development of cantilever-based biosensors, in particular the dynamic mode operation in liquid. This led to the contributions described in the next two chapters. Chapter 2 introduces a novel displacement sensor based on a squeezable molecular multilayer. This facilitates miniaturization of two of the most sensitive detection methods, and it allows operation in aqueous solutions. Chapter 3 presents inverted Chladni figures in microfluidics. A 200-year-old phenomenon was revisited to position micro- and nanoparticles on cantilever sensors. The driving force was acoustic streaming. The chapter starts with a section on the historic background, and concludes with a section on the physics of acoustic streaming, which is clarified here for the first time. The final chapter draws conclusions and gives recommendations for future work.

Chapter 2

A novel displacement sensor based on a squeezable molecular multilayer

In this chapter, a novel displacement sensor is presented, which allows two existing methods to be scaled down into microscale systems for the first time. The methods are tunneling readout and capacitive readout. The novel adaptation is the use of a squeezable insulator, which roughly defines the distance between the electrodes. For the tunneling sensor, this can circumvent the use of an alignment mechanism; for the capacitive sensor, it prevents the (planar) electrodes from snapping together. For both methods, proof-of-principle studies have been performed. These are presented in the next two sections 2.1 and 2.2.

2.1 Tunneling readout using molecular bilayers*

Introduction

In early versions of the atomic force microscope (AFM) [BQG86], the deflection was measured by a tunnel current. Although this is the most sensitive of methods, other methods are now usually preferred. A popular alternative is optical detection, which includes interferometry [SA89, RMG89], beam deflection [MA88, FBL00, FKK05], and interdigital detection [MMA96, SBF03]. These techniques achieve a good sensitivity, but have rather large space requirements because of the optical path lengths. Other methods include piezoresistive [TYB91] and thermal detection [BDD99], which are well integrated but produce heat. Capacitive readout [BBR96, DSB97] is simple, but can be limited by snap-in of the counter-electrode. There are also piezoelectric measurements [AAZ89], which have to be operated in dynamic mode, and readouts by superconducting single-electron transistors (SSET) [LBC04], which work only at low temperatures.

The reason that these methods are preferred over the use of a tunnel current is that the latter has its own disadvantages: the relatively involved alignment of the tunneling electrodes and their sensitivity to contamination. Both drawbacks originate from the presence of an air/vacuum gap between the electrodes. Clearly, these problems did not arise in the early tunneling experiments through semiconductors and oxides. More recently, imaging studies were performed by scanning tunneling microscopy (STM) on self-assembled monolayers (SAMs) [DMG94], and the conductances were studied by shear-force microscopy [FYC04].

*Part of this section is based on: *M. Dorrestijn, A. Bietsch, Ch. Gerber, and E. Meyer, "A tunneling displacement sensor based on a squeezable molecular bilayer", Nanotechnology 17 (2006) 2242–2245.*

In the tunneling displacement sensing technique presented here, a squeezable tunnel barrier substitutes the air/vacuum gap. The squeezable film consists of two stacked SAMs of alkanethiolate molecules. To provide proof of principle, a large-radius conducting AFM (C-AFM) tip was used to investigate the current vs. distance behavior (see figure 2.1). In potential applications, the conducting tip may be fixed and positioned against a bilayer on a deflecting surface. A vertical alignment mechanism can be omitted because the tunneling gap is predefined by the thickness of the film.¹

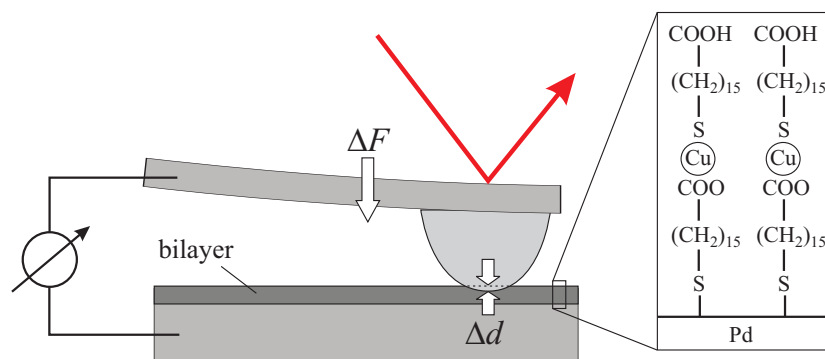


Figure 2.1: Schematic of the setup for electromechanical characterization of the 4-nm-thick bilayer (A). A large-radius Pt-coated AFM tip contacts the bilayer, which was grown on a Pd/Ti/Si substrate. Variation of the applied force (ΔF) causes a deformation of the bilayer (Δd), which leads to an exponential variation of a tunnel current. The force F is measured by laser-beam deflection.

Conducting AFM setup

To contact bilayers, tunneling electrodes having a large apex radius were used; commercial cantilever tips (NCHR-W, NanoSensors, Germany) were sputter-coated with 10 nm Ti and 180 nm Pt. The resulting radius was approximately 70 nm, as determined by scanning electron microscopy (SEM). The measured spring constant of the cantilever was 49 N/m. The sample was scanned using an x - y scan stage with capacitive feedback (P731.20, Physik Instrumente, Germany) allowing hysteresis-free absolute positioning with nanometer accuracy. The I - V converter was based on an OPA627 operational amplifier (Burr-Brown) and had a conversion ratio of 10^7 V/A, a bandwidth of 10 kHz, and a noise level of 0.16 nA_{rms} at open input. Further details on the C-AFM are described elsewhere [BSW00]. Three adaptations to the existing setup were made. Firstly, the setup was placed on a stack of rubber mats, each of a different stiffness (Fig. 2.2(a)). This reduced the noise level by an order of magnitude. Secondly, the system was rewired and reprogrammed to switch tapping mode off during each approach. This reduced the force exerted onto the bilayer film. Thirdly, the electronics were adapted as to allow tip voltages on the order of 1 V.

Prior to tunneling experiments, a topographic image of the sample region of interest was recorded operating the AFM in tapping mode (Fig. 2.2(d)). Current vs. distance measurements were carried out on individual spots of the bilayer. For each measurement, the tapping feedback was switched off, and the tip piezo was ramped from 0 to 100 nm. The tip-sample distance d was obtained from $d = d_o - (z_p - z_c)$, where z_p is the travel of the tip piezo, z_c the deflection of the cantilever, and d_o an offset to obtain $d = 0$ at the substrate. The contact force was determined from $F = kz_c$, k being the cantilever's spring constant. To improve the signal-to-noise ratio (SNR), the

¹Pending patent application in the United Kingdom, number UK 0512657.8 (May 19, 2005).

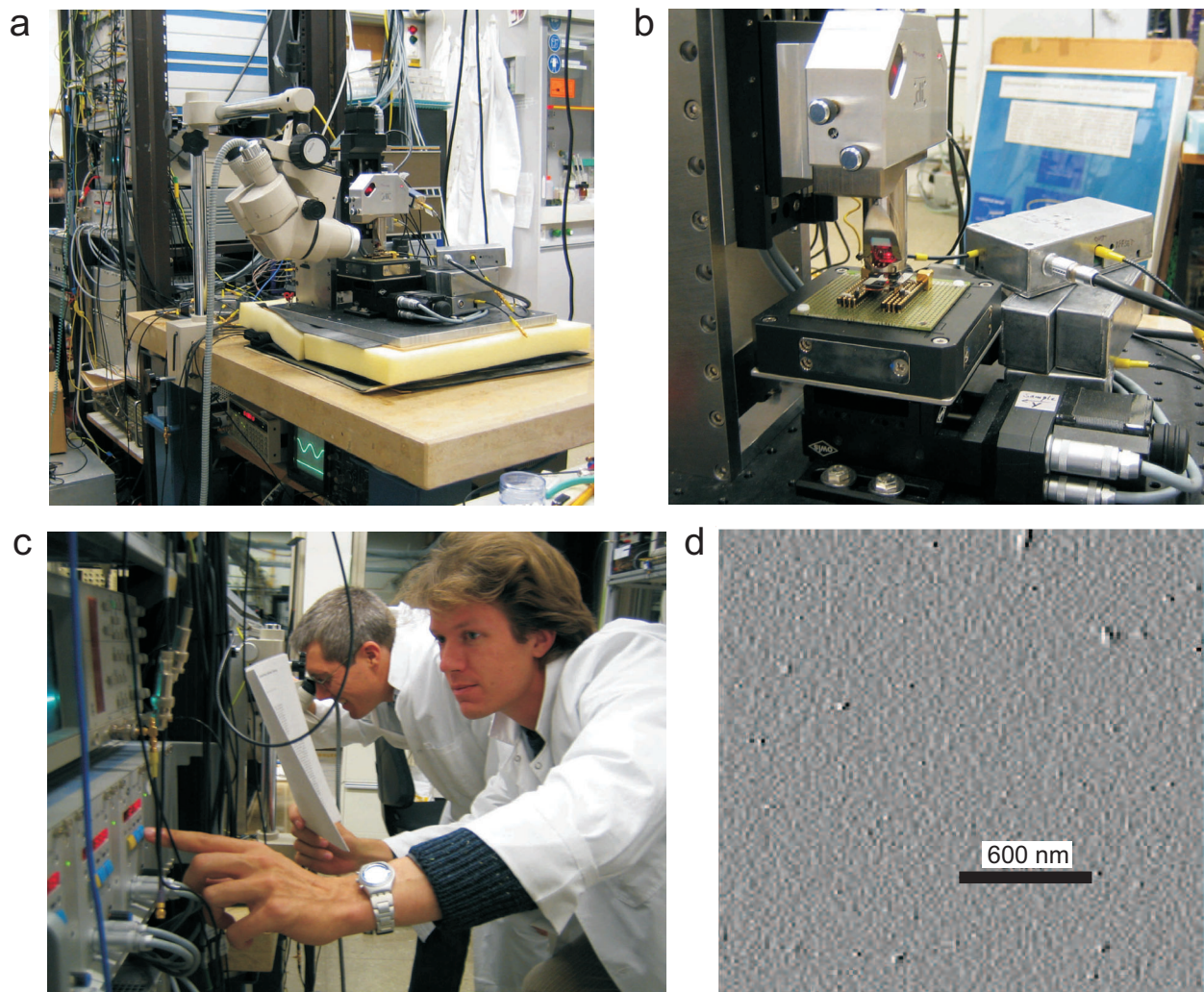


Figure 2.2: (a) The C-AFM setup. (b) Close-up showing a Veeco-DI Dimension head, coarse and fine x-y stages, and the I-V converter. (c) Dr. Alexander Bietsch and the author aligning the C-AFM tip with the surface. (d) A topography image was made prior to current measurements.

tip bias (vs. substrate) was set at +4.8 V, a relatively high voltage and close to the breakdown voltage of the bilayer. Measurements were performed 15 times at different locations to further improve the SNR.

Growth and characterization of self-assembled multilayers

The material of the squeezable insulator was a self-assembled multilayer. The advantage over a polymer film is that the latter cannot be produced thinner than around 50 nm by spin-coating. Self-assembled multilayers of mercapto-hexadecanoic acid (MHDA) were grown by the method of Evans *et al* [FEU95]. Copper ions are used as “glue” to stack the monolayers – they connect the carboxylic acid (COOH) moieties to the thiol (SH) groups of the next monolayer. Evans’ method was modified in two ways. Firstly, to reduce surface roughness, a palladium substrate was used instead of gold because of its smaller grain size [CGS02]. A 5-nm-thick palladium film was thermally evaporated (e-beam) at 0.11 nm/s onto a Si<100> wafer using a 2-nm-thick titanium adhesion layer (evaporated at 0.03 nm/s). Secondly, to increase the average domain size of the SAMs (thus reducing the number of defects) [DMG94], longer incubation times were used for the MHDA solution: 17–48 h instead of the 0.17–4 h used by Evans *et al*.

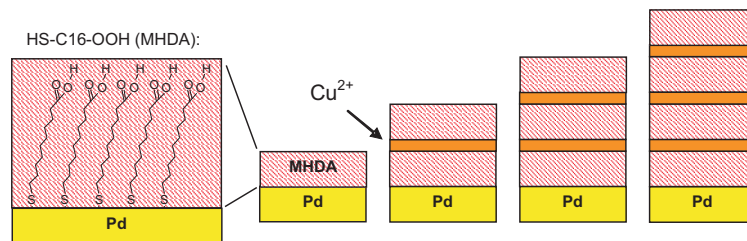


Figure 2.3: Monolayers of MHDA were stacked using copper ions.

Samples were stored under argon. Bilayers and tetralayers were grown for the tunneling experiments and thickness measurements, respectively. The thickness of a tetralayer was measured using AFM. A square area of the multilayer was removed by AFM lithography (applying 5 nN to a tip with a radius of ~ 10 nm), and the step height was determined by contact-mode AFM imaging (0.1 nN). Figure 2.4 shows the image and the corresponding height profile. The thickness of the tetralayer was determined to be 7.0 ± 0.3 nm, consistent with values obtained by Evans *et al* (6.6 nm, ellipsometry) and Hatzor and Weiss [HW01] (7.2 ± 0.2 nm, ellipsometry). No height reduction of the tetralayer was observed upon increasing the force from 0.1 to 0.4 nN, confirming the accuracy of the measured thickness.

Results and discussion

The results of the force and current measurements are shown in figure 2.5(a) and (b). The resistance of the bilayer was on the order of $5 \text{ G}\Omega$, 2 orders below typical values for monolayers [DMG94, FYC04]. This is in correspondence with the tip radius being ten times larger than that of typical imaging tips.

The conductance of a molecular tunnel barrier is – according to the Landauer formula – linearly dependent on the transmission function T_{mol} of the molecule, i.e. the efficiency of charge transport through the molecule. The tunnel barrier can roughly be approximated as being rectangular, in

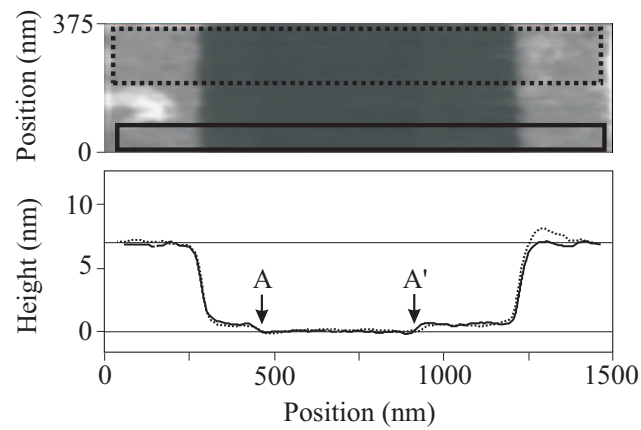


Figure 2.4: Contact-mode AFM image and the corresponding height profile of a MHDA tetralayer after AFM lithography. A square area was removed by scanning an AFM tip (radius ~ 10 nm) at high force (5 nN). In the area between A and A', the tetralayer was removed down to the palladium layer. The two curves are averaged scan lines in the two areas marked in the top image.

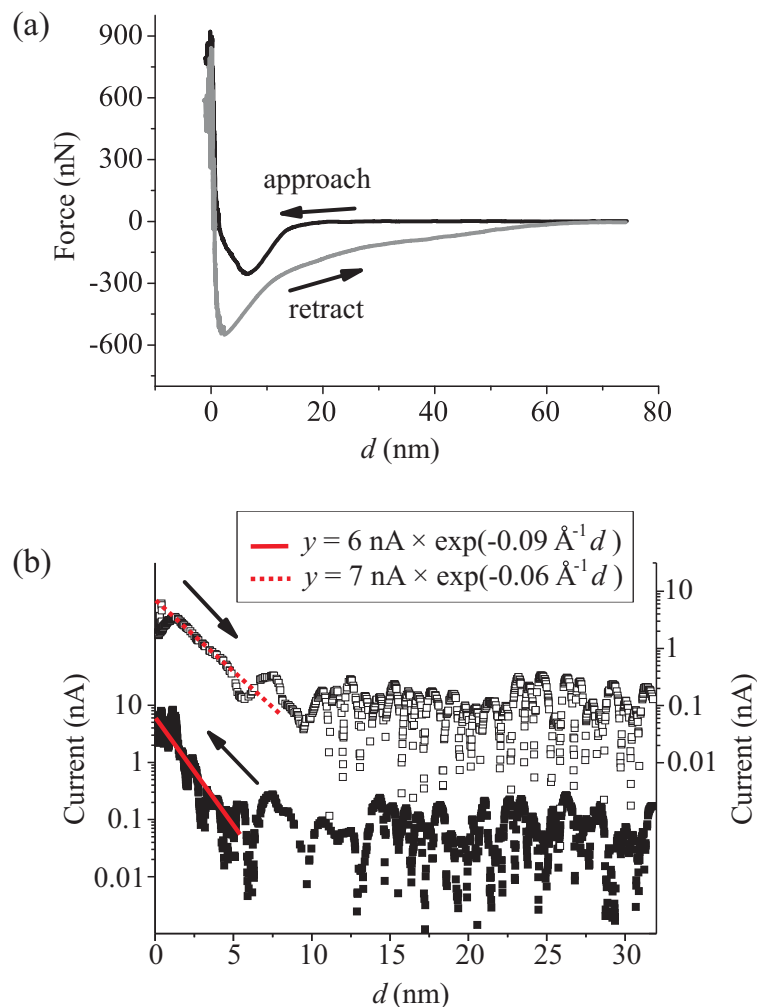


Figure 2.5: (a) Force vs. tip displacement curves and (b) current vs. tip displacement curves at +4.8 V tip bias (vs. substrate) on a MHDA bilayer. The two current vs. distance curves are vertically offset for clarity. The curves shown are averages of 15 approaches at different locations on the bilayer.

which case $T_{\text{mol}} = \exp(-\beta l)$, where l is the width of the barrier, i.e. the length of the molecule, and β is an inverse decay length given by [Sim63]

$$\beta \approx 2 \left[\frac{2m^*}{\hbar^2} (\Delta E - (eV/2)) \right]^{1/2}, \quad (2.1)$$

where ΔE is the energy difference between the Fermi level of the electrode and the closest molecular orbital, V is the bias applied across the molecule(s), and m^* is the effective electron mass.

The fitted lines in figure 2.5(b) yield a tunneling decay parameter β of $0.08 \pm 0.02 \text{ \AA}^{-1}$, defined in (1). The measured β (0.08 \AA^{-1}) is significantly smaller than typical values for alkanethiolate monolayers ($0.6 - 0.9 \text{ \AA}^{-1}$) [WLR05] and for monolayers of π -bonded molecules (0.4 \AA^{-1}) [WHR02]. This is likely due to the bias voltage being close to the breakdown voltage. When tunneling is close to resonance, β is relatively low, as seen from (1). In addition, we cannot exclude that the intermediate copper ions formed a localized state. Apart from coherent tunneling, electron transfer could then take place by the more efficient hopping mechanism [HR03], thus further reducing β .

The noise level in figure 2.5(b) reaches a value of $0.1 \text{ nA}_{\text{rms}}$ in the non-contact range. In sensor applications, the noise can be reduced electronically by integrating an adapted preamplifier. Mechanical noise would be lessened by the absence of an alignment mechanism and with smaller dimensions.

Immediately before the above current vs. distance experiments, I-V curves were recorded (same sample and the same tip). The results are shown in Fig. 2.6. Most curves were flat within the noise level, but several curves showed structure. Peaks showed at -2.5V and $+2.5\text{V}$, suggesting that the density of states of the surface was “imaged”. This might represent the band structure the MHDA bilayer. Fan *et al* [FYC02, FYC04] measured similar current peaks for alkanethiol monolayers. However, the peak currents we measured were exceptionally high: $10^{-9} - 10^{-7} \text{ A}$, which is three orders of magnitude higher than the peaks observed for the single monolayer of Fan *et al*. This is due to the larger contact area of the C-AFM tip; it was two or three orders of magnitude larger than the area of the sharpened Pt wires and the indium dendrites used by Fan *et al*. Why most I-V curves were flat within the noise, may be attributed to two factors: the high noise level of 3 nA , combined with the large variation in peak heights. In most measurements, the peaks may have been smaller than 3 nA . This large variation of peak currents can be due to the variation in the applied force: only the piezo distance traveled towards the surface was controlled (about 100 nm).

2.2 Capacitive readout using molecular multilayers

Introduction

A relatively simple method to measure displacement is the use of a capacitor [BMB91]. This method has been limited, however, by the tendency of the electrodes to snap together (“snap-in”) [DAH03]. This presents a lower limit to the distance between the electrodes, or an upper limit to the electrostatic force that may be applied.

We present for the first time a method for preventing snap-in. A squeezable dielectric fills

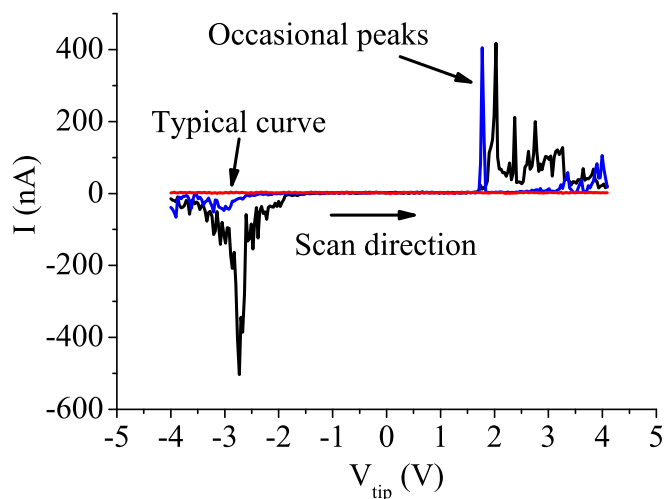


Figure 2.6: I-V curves recorded at different locations of the bilayer MHDA surface. Shown is a typical curve (red), which is flat within the noise of 3 nA. At several occasions (black and blue), however, current peaks were seen around -2.5V and +2.5V. These could represent the density of states at the surface.

the gap between the electrodes.² To illustrate this, Fig. 2.7 shows a schematic of an application for scanning probe microscopy. The use of a self-assembled multilayer as a dielectric has been assessed. Firstly, fabrication of a top-contact has been investigated. Secondly, using a top-contact, the dielectric constant of the film was measured.

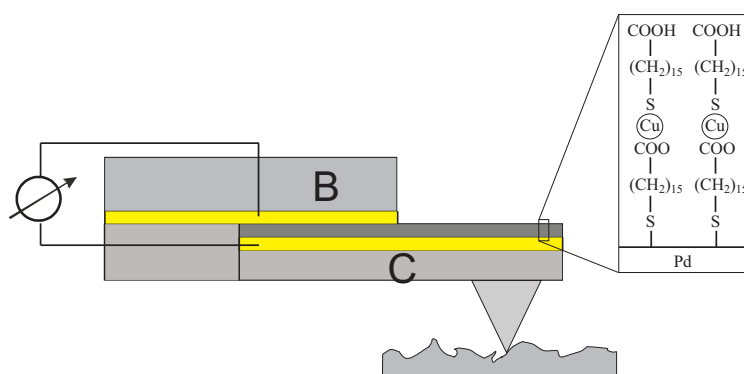


Figure 2.7: An integrated device measures deflection of an SPM cantilever. The sandwich structure of the capacitive sensor consists of a cantilever (C) a self-assembled multilayer, and a fixed support (B). Electrodes are shown in yellow.

Multilayers with gold top contacts

Self-assembled monolayers and multilayers of mercapto-hexadecanoic acid were produced as described in Section 2.1.

²Pending patent application in the United Kingdom, number UK 0512657.8 (May 19, 2005).

Gold top contacts were evaporated onto mono- and multilayers through shadow masks. Smaller contacts were preferred as to reduce the chance of shortcircuits. Masks for mm-sized contacts were made from Kapton foil.³ In the foil, arrays of differently-sized holes were drilled: 2, 1, and 0.5 mm. Masks for 300-nm contacts were microfabricated from Si/SiN wafers. Rectangular areas ($100 \times 70 \mu\text{m}^2$) were locally wet-etched up to the nitride, leaving a membrane. The membrane contained 300-nm holes generated with a focussed ion beam (FIB). The SiN was placed in contact with the sample during evaporation. Surface unevenness and incidental dust particles created a gap on the order of a micrometer; direct contact was thus prevented.

The 300-nm contacts were contacted with a C-AFM probe; the setup is the same as described in Section 2.1, but without the three adaptations mentioned there. After imaging the surface in tapping mode, 100 approaches were made at equidistant positions along a selected line. During each approach, an I-V curve was recorded. During approaches, the tapping excitation remained active, but the cantilever amplitude was seen to be zero during contact.

The millimeter-scale contacts could be contacted with a drop of mercury. Advantages of the mercury contacts were absence of film compression by a solid tip, and the higher speed at which experiments could be repeated.

Setup with mercury top contact

The second setup uses a drop of mercury as a top-contact (Fig. 2.8(a), (b)). The mercury was hung from a gold probe (Fig. 2.8(b)). The probe was connected to a coaxial cable, which was clamped at the base by a micromanipulator (Leika). Thus, the droplet could manually be positioned onto the multilayer surface, or on a gold top contact.

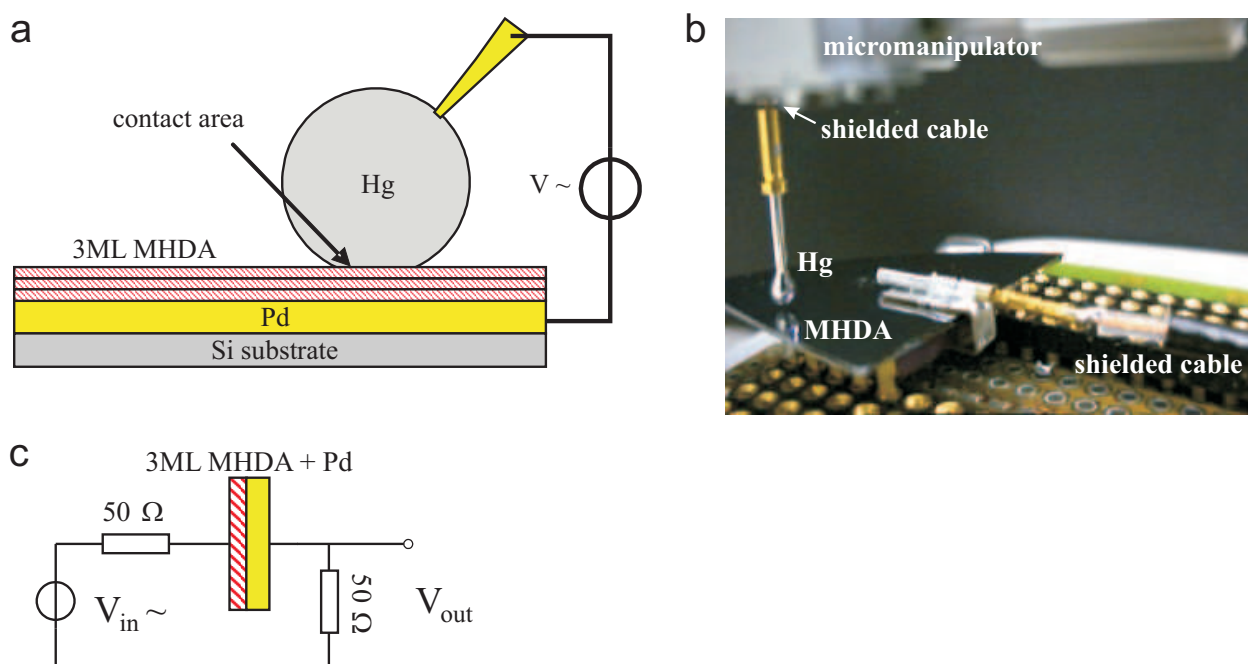


Figure 2.8: (a) The setup used for measuring capacitances of self-assembled multilayers. (b) Schematic of the setup. (c) The corresponding circuit.

The dielectric constant of a trilayer was determined by measuring the impedance (circuit shown

³Kapton foil is a polymer sheet without significant degassing in vacuum.

in Fig. 2.8(c)). It was preferred not to measure impedance simply at one AC frequency. Rather, full spectra were acquired using a network analyzer (Hewlett Packard HP3589); this was done in order to identify unwanted inductances or capacitances in the measurement circuit. First, the unknown resistance of the palladium film (R_f) was determined as follows:

$$\frac{50\Omega}{50\Omega + Z} = \frac{V_{out}}{V_{in} + V_{out}} \quad (2.2)$$

$$Z = R_f + \frac{1}{j(2\pi f)C}. \quad (2.3)$$

For $f \rightarrow \infty$, the (still) unknown capacitance C is removed from the equation: $Z = R_f$. Experimentally, this was done by extrapolating the frequency spectrum. Next, the 3-dB frequency of the spectrum was used to calculate the dielectric constant ϵ_r as follows.

$$f_{3dB} = \frac{1}{2\pi RC} \quad (2.4)$$

$$R = 2 \times 50\Omega + R_f \quad (2.5)$$

$$C = \epsilon_o \epsilon_r A / d \quad (2.6)$$

$$\Rightarrow \epsilon_r = \frac{d}{2\pi f \epsilon_o A (R_f + 100\Omega)}, \quad (2.7)$$

where ϵ_o , A , and d are the permittivity of vacuum, the contact area of the mercury, and the thickness of the multilayer, respectively. The area A was measured by holding calipers close to the base of the droplet.

In the initial setup, an unwanted inductance was observed in the spectra (Fig. 2.12). This came from the internal inductance of the wires. The coaxial cables had an impedance of 50Ω ($Z = \sqrt{L/C} = 50\Omega$). In other words, in such cables, the inductance is normally compensated by the capacitance. In the initial setup, however, the capacitance was reduced, leaving an exposed inductance. The reduction of the capacitance had two causes. Firstly, there was a 10-cm gap in the shielding near the contacts to the multilayer. As a solution, coaxial cables were brought as close as possible to the experiment (Fig. 2.9). Secondly, it was calculated that at the applied RF frequencies, the electromagnetic wavelength was comparable to the total length of the cables.⁴ This causes the current in the cable shielding to flow in opposite directions at different positions along the cable. This again reduces the effectiveness of the shielding, making the internal capacitance smaller. As a solution, the shields were grounded at two additional positions: just before and just after the experiment. A metal plate served as the (AC) ground (Fig. 2.9).

The accuracy was further improved in two ways. Firstly, most stray capacitance to the surroundings was removed.⁵ To achieve this, a grounded L-shaped metal plate was integrated into the setup (Fig. 2.9).⁶ Secondly, the network analyzer was calibrated before each measurement in the following way. First, the drop of mercury was shorted to the clamp contacting the palladium substrate. Then, the network analyzer generated a spectrum and was instructed to compare all the following measurements to this blank. Thus, only differential measurements were made.

⁴The vacuum wavelength was as short as $c/f = (3 \times 10^8 \text{m/s}) / (3 \times 10^7 \text{Hz}) = 10 \text{m}$. Inside BNC cables, the velocity of the electromagnetic field is about 70% of light speed, giving a wavelength of about 7m. The total length of the cables was comparable: about 2 m.

⁵Objects in the vicinity can vary their position (e.g. a person). Also, they may carry an AC potential (e.g. 50 Hz), which capacitively couples to the circuit.

⁶In that way, field lines originating at the unshielded contacts would lead mainly to the L-shaped plate. Although the thus generated ground loop can pick up AC fields, this could at most generate a few constant spikes in the spectrum.

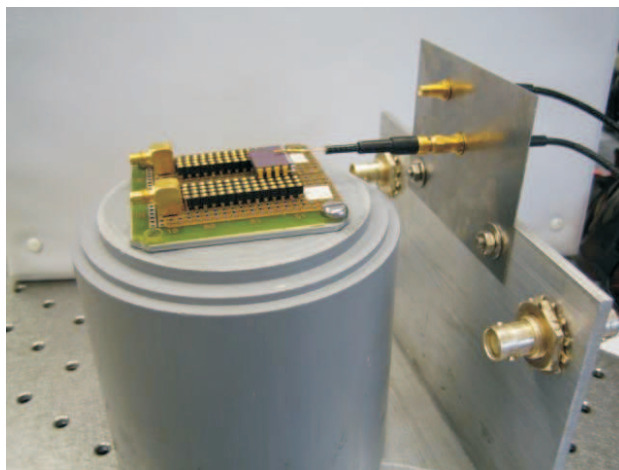


Figure 2.9: Part of the improved setup showing L-shaped metal shielding and a coaxial cable leading as close as possible to the experiment.

Results and discussion

The 300-nm gold top contacts were evaporated onto monolayers of MHDA. An AFM image is shown in Fig. 2.10. C-AFM measurements show that the evaporation had caused electrical shorts through the monolayer (Fig. 2.11). The resistance between the gold top contact and the Pd substrate is only 175Ω . Interestingly, the resistance measured in-between gold contacts is not much higher. This could have two causes. Firstly, lateral forces exerted by contact-mode C-AFM imaging could have damaged the monolayer. Secondly, the phase image of Fig. 2.10 shows the same phase for the SAM-covered grains of the gold islands and the grains seen in-between gold islands. This suggests that during evaporation, some of the gold reached the areas covered by the mask. Due to the elevated temperature and the high mobility of gold structures, electrical shorts could have formed there as well.

In the setup with the mercury top-contact, the electronics had to be improved. As shown in Fig. 2.12, an unwanted inductance was observed in the spectra. Four improvements were implemented before further experiments were conducted. These improvements are described in the previous section.

The mercury top-contact was first applied to verify the C-AFM measurements. Tetralayers with gold top contacts of 0.5-2 mm were used. When the Hg drop was held on top of a gold contact, a short was observed, in correspondence with the C-AFM measurements. However, after the drop was dragged onto the bare tetralayer, a different spectrum was observed (Fig. 2.13). Then a first-order high-pass characteristic showed, which corresponds to a single capacitor. The capacitor was formed by the insulating multilayer. The mercury slid cleanly over the gold and the multilayer surfaces, without sticking.

From the measured spectra, the dielectric constant of a trilayer could be determined. Fig. 2.14(a) shows two spectra corresponding to different contact areas A . The 3-dB points are 1 and 3 MHz for $A = 0.4\text{mm}^2$ and $A = 0.13\text{mm}^2$, respectively. The area was controlled by the height of the gold electrode holding the mercury. To calculate ϵ_r from these frequencies using Eq. 2.7, the resistance R_f of the Pd film has to be determined. From Fig. 2.14(b), it follows that for $f \rightarrow \infty$, $|V_{out}/V_{in}| = 0.6$. So $R_f = 67\Omega$ (Eq. 2.2). The thickness of a tetralayer was measured in Chapter 2.1; it was 7.0 nm, which implies 5.3 nm for the trilayer. According to Eq. 2.7, this results in $\epsilon_r = 1.48$ and $\epsilon_r = 1.51$ for 1 and 3 MHz cutoff frequencies, respectively. This is smaller

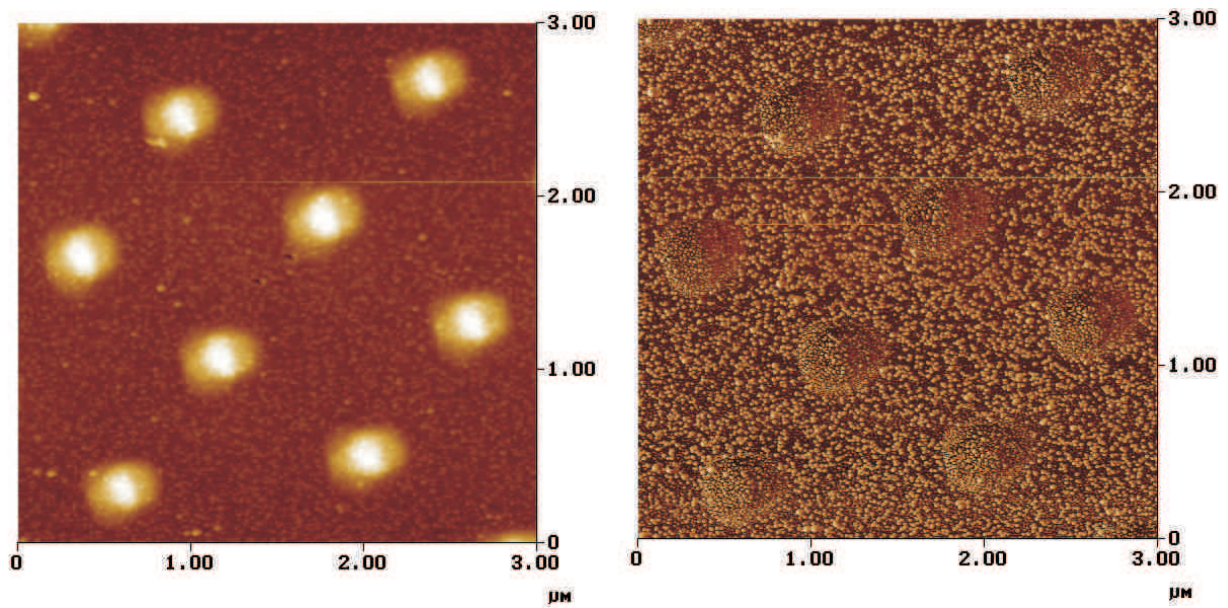


Figure 2.10: AFM height image (left) and phase image (right) of the 300-nm gold top contacts. The substrate is Pd with a MHDA monolayer.

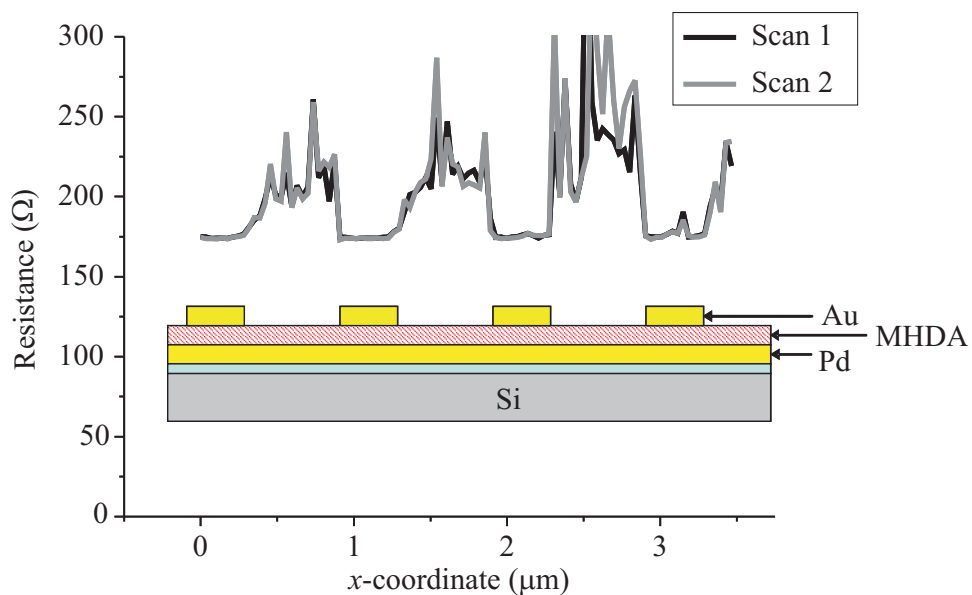


Figure 2.11: Resistance measurements performed with C-AFM. The tip was scanned along the structure shown in the inset (gold top contacts are yellow).

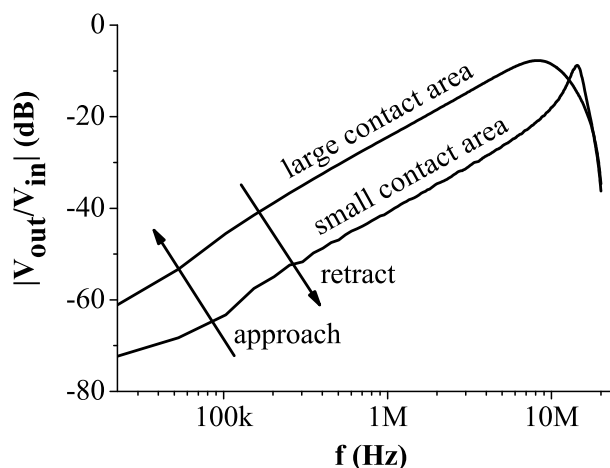


Figure 2.12: Bode plot for the initial setup. An MHDA trilayer is contacted by a drop of Hg. The two graphs correspond to different contact areas. As expected, the capacitance of the trilayer gives a slope of +20 dB/decade (first-order high-pass characteristic). However, unwanted inductance in the wires causes a steep negative slope beyond $f = 1/(2\pi\sqrt{LC})$.

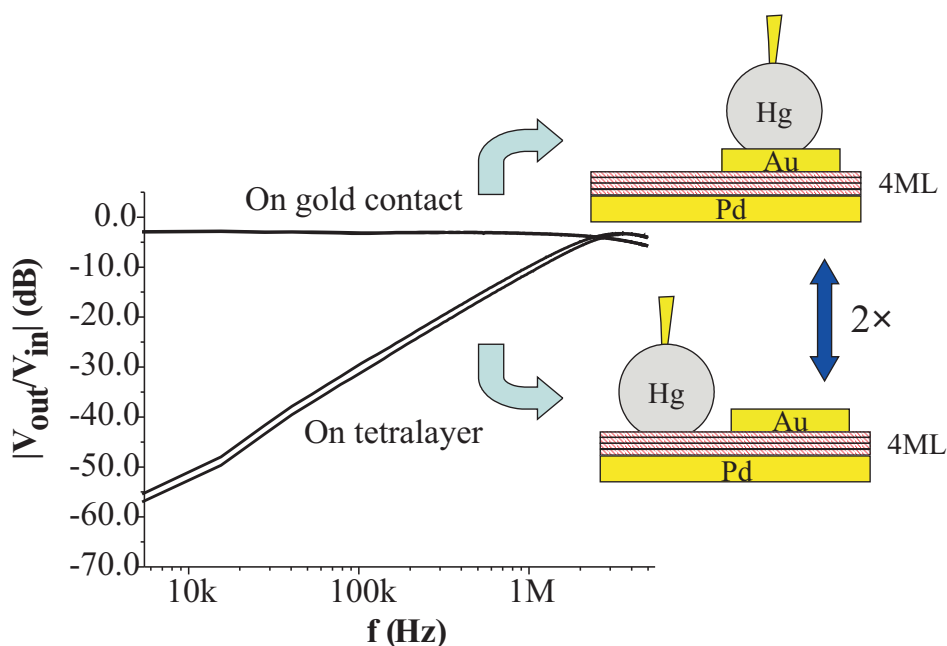


Figure 2.13: Bode plots recorded for tetralayer films of MHDA. 1-mm gold contacts had been evaporated onto the film. A drop of Hg was dragged laterally on and off a gold contact two times. Spectra reproducibly show 1st-order high-pass behavior on the bare tetralayer. On the island, however, a short-cut is seen.

than the dielectric constant of alkanathiolate SAMs, which is around 2.6 [PBA87, RSW98]. The discrepancy might be caused by the presence of the copper ions.

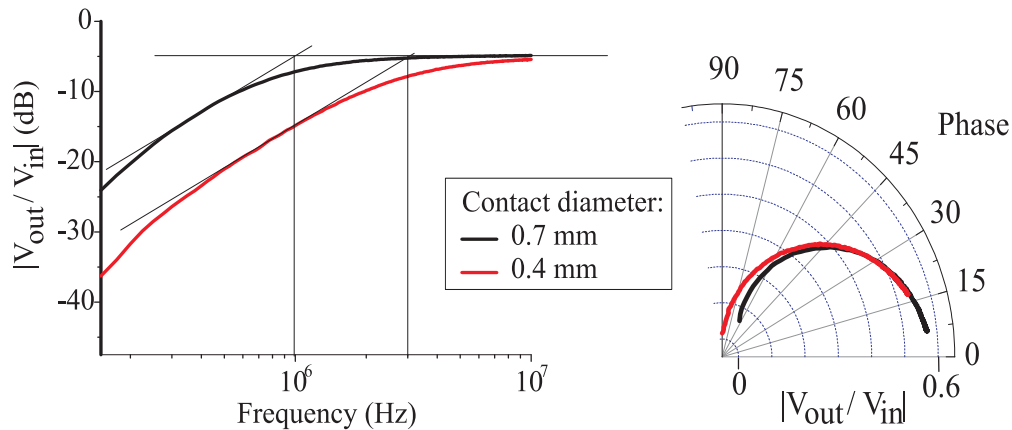


Figure 2.14: Bode plots for a trilayer of MHDA; the two curves correspond to different contact areas of the drop of mercury.

For the first time, the dielectric constant of a self-assembled multilayer was measured. Using a mercury top contact, it was found that $\epsilon_r = 1.5$. This is smaller than the dielectric constant of alkanethiolate SAMs (2.6), which might be due to the integrated copper ions. These results are the first step towards a capacitive displacement sensor that is insensitive to snap-in.

Implementation into a sensor

Alternatives to self-assembled multilayers are spin coating and surface-initiated polymerization (SIP). Different insulator thicknesses may be selected depending on the range of translation. Film thicknesses of 2 to 20 nm can be built up from the multilayers described in this section. Films thicker than 50 nm can be made by spin-coating polymers; these are preferably low-modulus polymers to limit the force required for indentation. Films of intermediate thickness (5-50 nm) can be grown by SIP using oligo(ethylene glycol), as recently described by Ma *et al* [MHS04].

A solid top contact (as opposed to the liquid drop of mercury) could be produced in one of the following four ways. The first method consists of inkjet printing a liquid pattern onto the insulating film [SKF00, BZH04]. The liquid could be a suspension of metal particles, forming a deposit upon drying, or it could be a solution of complexed metal ions that are deposited by action of a reducing agent, which is known as electroless deposition (ELD). The second method comprises transfer of a catalyst onto the film via microcontact printing (μ CP) from a soft stamp, followed by electroless deposition (ELD) of a metal. The third method is to stamp a metal contact directly onto the film. The fourth method comprises floating a patterned metal film off a master in a liquid bath and subsequently transferring it to the film by micromanipulation - a technique commonly used in transmission electron microscopy (TEM).

The capacitance can be determined from the impedance at a single frequency only using $I = d(CV)/dt = CdV/dt$. It can be even easier when the displacement is oscillatory: then a DC voltage results in AC current according to $I = d(CV)/dt = VdC/dt$.

Chapter 3

Nanomechanical resonators generating Chladni figures and acoustic streaming

3.1 A brief history of Chladni figures and acoustics

It seems appropriate to open this chapter with a quotation from Michael Faraday [Far31]:

The beautiful series of forms assumed by sand, filings, or other grains, when lying upon vibrating plates, discovered and developed by Chladni, are so striking as to be recalled to the minds of those who have seen them by the slightest reference.

Ernst Florens Friedrich Chladni (1756-1827), a German musician and scientist, was first trained in law at the University of Leipzig, but soon turned to physics. His interest in music was reflected in his main research topic. He did many experiments on the vibrations of plates and showed how these could be made visible by sprinkling sand over the vibrating surface. When exciting a metal plate with a violin bow, the sand could be seen to gather along the nodal lines where there was no motion. These have long been known as Chladni figures. Chladni's most important books are *Entdeckungen über die Theorie des Klanges* (1787) [Chl87] and *Die Akustik* (1802, second edition 1830) [Chl02]. A complete list of his works is given by Melde, in *Chladni's Leben und Wirken* [Mel88], a book now very rare.

In 1802, Chladni went “on tour” through Europe to demonstrate this fascinating phenomenon, undisturbed by the wars that were going on. He lectured at European courts and to important personages. When the Emperor Napoleon received a personal demonstration, he was so delighted, that he financed a translation of *Die Akustik* into French. The translation was to be done by Chladni, and the *Traité d'Acoustique* appeared in 1809 [Chl09]. Napoleon also provided for the Institute of France a prize of 3000 francs to be awarded for a satisfactory mathematical theory of the vibrations of plates. This was finally awarded in 1815 to the mathematician Sophie Germain,¹ who gave the correct fourth-order differential equation for plate vibrations (although her choice of boundary conditions was incorrect [Lin66]). Mlle. Germain apparently corresponded with Gauss under the *nom de plume* “Mr. Leblanc”, a not uncommon custom for women of letters in that day [Bel53].

The physical origin of sound had long been known, though. The ancient Greek philosophers were already convinced that sound is produced by the motion of objects, and that it is transmitted by (some undefined) motions of the air. It is usually assumed that the first Greek philosopher to study the origin of musical sounds was Pythagoras, who established his school in Crotona in

¹Chladni gives the date as January 6th, 1816 [Chl17].

southern Italy in the 6th century B.C. He discovered that of two stretched strings of lengths L and $2L$, the shorter will emit a note an octave above the other [CD48]. It was Aristotle (384–322 B.C.), student of Plato and teacher of Alexander the Great, who understood that air was the transmitting medium. He wrote in his work *De Anima* (On the Soul), book II [CD48]:

Hence the air must be struck quickly and forcibly if it is to give forth sound; for the movement of the striker must be too rapid to allow the air time to disperse (...) That, then, is resonant which is capable of exciting motion in a mass of air continuously one as far as the ear. There is air naturally attached to the ear. And because the ear is in the air, when the external air is set into motion, the air within the ear moves.

Aristotle's theory was not confirmed experimentally until 1660, when Robert Boyle (1627–1691) rang a bell in a jar that he slowly evacuated [Boy82].

Knowing that the air is a sound-transmitting medium, the question at once arises: How rapidly does the propagation take place? As early as 1635, Gassendi [Len51], while in Paris, made measurements of the velocity of sound in air using firearms and assuming that the light of the flash is transmitted instantaneously. His value came out to be 1473 Paris feet per second or 478 m/s in the metric system (which was not introduced until the time of the French Revolution). The measurement suffered, however, from lack of reference to temperature, humidity, and wind velocity. The modern value for dry air of 20°C is 343.4767 m/s (for a 20-Hz tone) [Lid94]. The velocity of sound in liquid was first measured by the Swiss physicist Daniel Colladon (1802–1893). In 1826, he conducted studies in Lake Geneva; he was trying to win a prize competition organized by the Academy of Sciences in Paris. The subject of the competition was the measurement of the compressibility of the principle liquids. At first, Colladon used a direct method to statically measure the compressibility of water and several other liquids. He must have been fascinated by the relatively low values, and decided to obtain the value for water also indirectly via the speed of sound. He thus obtained compressibility was very close to his directly measured value. His results appeared in the famous “Mémoire sur la compression des liquides et la vitesse du son dans l'eau”, which was awarded the Grand Prize of the Academy [CS27]. More details about this story can be found in his autobiography [Col93]; he describes for example the troubles he encountered in carrying the powder needed for his light flashes across the border between Switzerland and France. Physical properties of air and water are needed for the application of theories like the Navier-Stokes equation. This equation would lead to the understanding of one of the most puzzling observations of Chladni, as will be described shortly.

Chladni was actually not the first to observe Chladni figures. In 1638, Galileo Galilei mentioned a rudimentary pattern of this kind in his *Mathematical discourses concerning two new sciences*. The excerpt in Fig. 3.1 is a translation from 1730 [Lin73].

Chladni was, however, the first to report on ‘Faraday powder figures’, which were later explained by Michael Faraday (1791–1867). Normally, Chladni saw sand bounce off the points of maximal amplitude towards the nodal lines. However, he suddenly noticed how fine shavings from the hairs of the violin bow moved in the opposite direction. He was never able to uncover the mystery. In 1831, it was finally Faraday who explained it phenomenologically as being due to an induced airflow parallel to the surface [Far31]; such a flow is now known as acoustic streaming. Faraday had repeated Chladni's experiments using lycopodium powder.² By attaching pieces of

²Lycopodium powder is a fine yellow powder derived from the spores of *Lycopodium clavatum*. It is characterized by a relatively large surface-to-volume ratio. This is also the reason for its past use in explosives and fireworks. When the powder is dispersed into a fine mist near a candle flame, it ignites into a spectacular fireball.

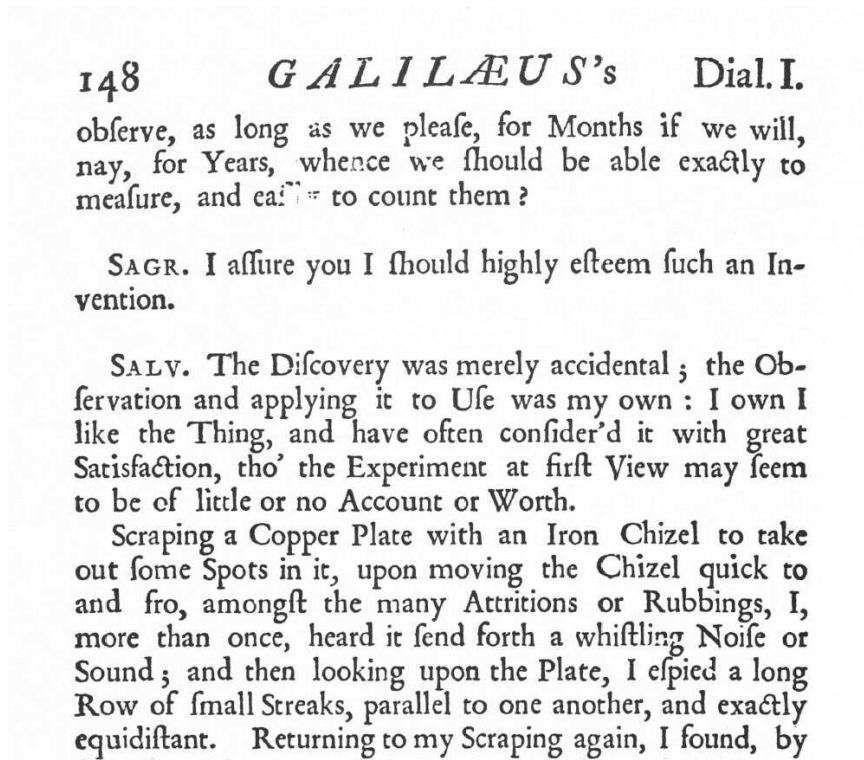


Figure 3.1: Excerpt from Galileo Galilei's *Mathematical discourses concerning two new sciences relating to mechanicks and local motion, in four dialogues*. Shown is page 148 of a translation of Dialog I, printed in 1730. It describes Galilei's discovery of Chladni figures 160 years before Chladni did. Here, *Sagr. and Salv.* stand for the names of two late friends of Galilei's, whom he wanted to make immortal. The dialogs between the two were fictitiously held over four days in the Palazzo Sagredo in Venice, at the Canal Grande.

paper to the surface of the plate, he could redirect the air flow; he then studied how the fine-powder figures were modified. However, Faraday could not say how this flow was induced.

It was Lord Rayleigh³ (1842–1919) who analytically explained the airflow in 1884 by solving the Navier-Stokes equation for such type of system [Ray84]. This was one of his many notable achievements.⁴

Robert Hooke (1635–1703), well-known for his law of elasticity, showed movements of air in a vibrating glass bell using fine powder. In Dr. Birch's *History of the Royal Society* [Bir56, Bir57] we read:

Mr Hooke produced his glass bell with flour in it, to show to the eye, that according to the several strokes or pulses made upon the glass, the air thence receives as many several impressions, (...) Sir Christopher Wren coming in said, that the glass would vibrate much stronger, being struck on the edge with a viol-bow. This was also tried.

Leonardo da Vinci (1452-1519) wrote [Mac38]:

I say then that when a table is struck in different places the dust that is upon it is reduced to various shapes of mounds and tiny hillocks. (...) The dust descends from the hypotenuse of these hillocks, enters beneath their base and raises itself again around the axis of the point of the hillock.

³His full name was actually The Right Honourable John William Strutt, 3rd Baron Rayleigh.

⁴His discovery of the element argon earned him the 1904 Nobel Prize for Physics. He also discovered the phenomenon now called Rayleigh scattering and predicted the existence of the surface waves now known as Rayleigh waves.

3.2 Chladni figures in microfluidics*

In recent years, there has been increasing interest in the positioning of micro- and nanoparticles on surfaces. Applications include biosensors [LPM02, WN06] and molecular electronics [KBB03, Sem05]. For automated patterning of particles, existing methods are either slow (e.g. dip-pen lithography [LPM02, ZBC02]) or require prefabricated patterns (e.g. by electrostatic positioning [LB03] or by successive self-assembly, transfer, and integration (SATI) [KMD05]). Moreover, the sorting of differently-sized particles, organelles, and cells in microfluidic networks is important for many biological and medical applications. Purely size-based sorting would offer the greatest control, but an automated method appears to be inexistent. Current methods sort particles based on density and size (size-selective precipitation (SSP) [MNB93], ratchets [RER05] and the “Brazil nut effect” [RSP87, HR04]), surface properties and size (high-performance liquid chromatography (HPLC) [FWK89]), charge and size (gel electrophoresis [EKW90]), dielectric constant and size (dielectrophoresis [GM98, LB02]), and acoustic impedance and size (ultrasonic separation [ALL03]).

In 1787, the German physicist Chladni showed how sand particles could be made to self-organize into symmetrical patterns [Chl87]. Upon excitation of a metal plate with a violin bow, the sand on it would group along the nodal lines. The patterns, which vary with different modes of resonance, were named Chladni figures. Chladni also reported how fine particles (fine shavings from the hairs of his violin bow) would move in the opposite direction, to the antinodes. The latter behavior was found by Faraday [Far31] to be due to induced air currents, now known as boundary streaming.

Acoustic streaming is a steady circulatory flow that can be generated in oscillating fluids. The oscillation can be driven by a sound field in a compressible medium (“quartz wind”) or by an oscillating surface in a viscous medium (“boundary streaming”) [Nyb98, Ril01]. The latter results from the convective inertia term of the Navier–Stokes equation, which has a nonzero time-average. Boundary streaming near oscillating beam structures has recently gained interest in the context of air cooling for portable electronics devices [ARG03, LNB05].

In this work, microscale Chladni figures are presented for the first time. It is shown that nanoscale oscillations of cantilever beams in liquid drive particles initially resting on the surface to the nodes or to the antinodes, depending on their size. Similar to Faraday’s findings, the size-dependency resulted from boundary streaming. The formation of symmetrical patterns offers a cost-effective method for nanofabrication compared to lithographic techniques. In addition, the results imply the possibility of size-based sorting of micro- and nanoparticles.

Experimental

The experiments were performed in a PMMA (polymethylmethacrylate) microfluidic cell (100 μL , Fig. 3.3(a)) filled with water, and observed using dark-field microscopy. Silicon cantilever arrays of $560 \times 100 \times 7 \mu\text{m}^3$ (fabricated at the IBM Zurich Research Laboratory) were piezoelectrically actuated inside the cell. The resonance frequencies and amplitudes of the cantilevers were determined in liquid by laser beam deflection [MA88] using the head of a Nanoscope III microscope (Veeco-DI, see Fig. 3.3). Temperature increases from the laser and the piezo actuation did not

*Part of this section is based on: *M. Dorrestijn, A. Bietsch, T. Açıkalin, A. Raman, M. Hegner, E. Meyer, and Ch. Gerber, "Chladni Figures Revisited based on Nanomechanics", submitted (2006).*

affect the resonance frequencies significantly.⁵ Thiol-functionalized polystyrene beads (Merck-Estapor, France) with a ferrite core (iron(III)oxide) were size-selected by centrifugation to obtain batches of $4\pm 1\ \mu\text{m}$ (microbeads) or $0.5\pm 0.3\ \mu\text{m}$ (nanobeads), as determined by scanning electron microscopy (SEM, see Fig. 3.2). The observed diameter of the ferrite core was a fraction 0.54 ± 0.06 of the total bead diameter, giving a density of $1.7\pm 0.2\ \text{g/cm}^3$.⁶ In the microfluidic cell, the micro- and nanobeads settled by gravity within 20 or 120 min, respectively. Subsequent excitation of the cantilevers was performed at sequential resonance modes while observing with dark-field microscopy (Nikon Optiphot 200 equipped with a digital Sony DCR-PC330E PAL film camera for the microbeads and a digital Nikon microscope camera for the nanobeads). A new cell design with a five-times smaller volume (Fig. 3.3(c) and (d)) allowed for smaller microscope working distances. It was successfully tested using other types of micro- and nanobeads (results documented in the digital lab journal).

The well-known macroscopic Chladni figures were reproduced for demonstration purposes only. Course salt grains and fine grains were sprinkled on top of a metal plate ($15\times 15\text{cm}^2$) in air, which was clamped in its center by a metal pin. The pin was actuated by a loudspeaker driven by an analog function generator. For the fine grains, several powders were selected: $90\text{-}\mu\text{m}$ silicate glass spheres, fine kitchen salt (average size $60\ \mu\text{m}$), and powder sugar (average size $20\ \mu\text{m}$).

Results and discussion

The classical generation of Chladni figures yielded the following results. For course salt grains, sweeping of the excitation frequency produced the figures shown in Fig. 3.4, at 0.45, 0.85, 2.7, 3.6, 5.2, and 6.5 kHz, respectively. Of the fine powders, glass spheres and fine salt grains generated the same patterns as the course salt. The powder sugar, however, was seen to collect on the antinodes, as shown in Fig. 3.5. This is the phenomenon Chladni observed with the shavings from his violin bow (Chapter 3.1).

For the microcantilevers, the resonance frequencies of the first six resonance modes ranged from 12 kHz to 1.3 MHz. The corresponding vibration amplitudes ranged from 400 down to 8 nm. For modes 3–6, $4\text{-}\mu\text{m}$ beads were seen to move towards the antinodes of vibration, forming well-defined groups within 20–25 s.⁷ Groups could be repositioned by switching to a neighboring resonance mode, as demonstrated in Fig. 3.6(a). The positions of the antinodes were confirmed by direct observation of the locations of edge vortices containing trapped beads (see Fig. 3.7; this phenomenon has been demonstrated for liquid [SL01] and for air [LNB05]).

The $0.5\text{-}\mu\text{m}$ beads, however, moved towards the nodes, as shown in Fig. 3.6(c). Pattern formation took significantly longer, namely 13–17 min. The opposite directionality of differently-sized beads can be explained by assuming that the beads are dragged by boundary streaming. In air, the classical Chladni figures formed when sand particles bounced off the antinodes and came to rest on the nodes. Only for fine powder were the lateral inertia forces dominated by the viscous

⁵The temperature of the liquid affects viscosity and density of the water was monitored close to the cantilevers using the thermometer shown in Fig. 3.3(a). It was of the Pt100 type (a $100\text{-}\Omega$ platinum resistor, Heraeus Sensor Technology GmbH), which offered small packaging and high accuracy (tolerance class 1/3 DIN B, i.e. an uncertainty of $0.1\ ^\circ\text{C}$ from $0\text{--}100\ ^\circ\text{C}$). The thermometer's resistance was monitored by a source meter (Keithley Ke2400) using the four-point method. The source meter was controlled by a data-acquisition card (National Instruments 6031E) and LabVIEW 7.0 software (National Instruments) as to make a continuous series of measurements.

⁶The densities of iron(III)oxide and polystyrene are 5.2 and $1.05\ \text{g/cm}^3$, respectively.

⁷For the second mode, edge vortices dragged the $4\text{-}\mu\text{m}$ beads off the edges of the cantilever before grouping could be observed. Edge vortices were more pronounced for modes with larger node-node distances (lower mode numbers).

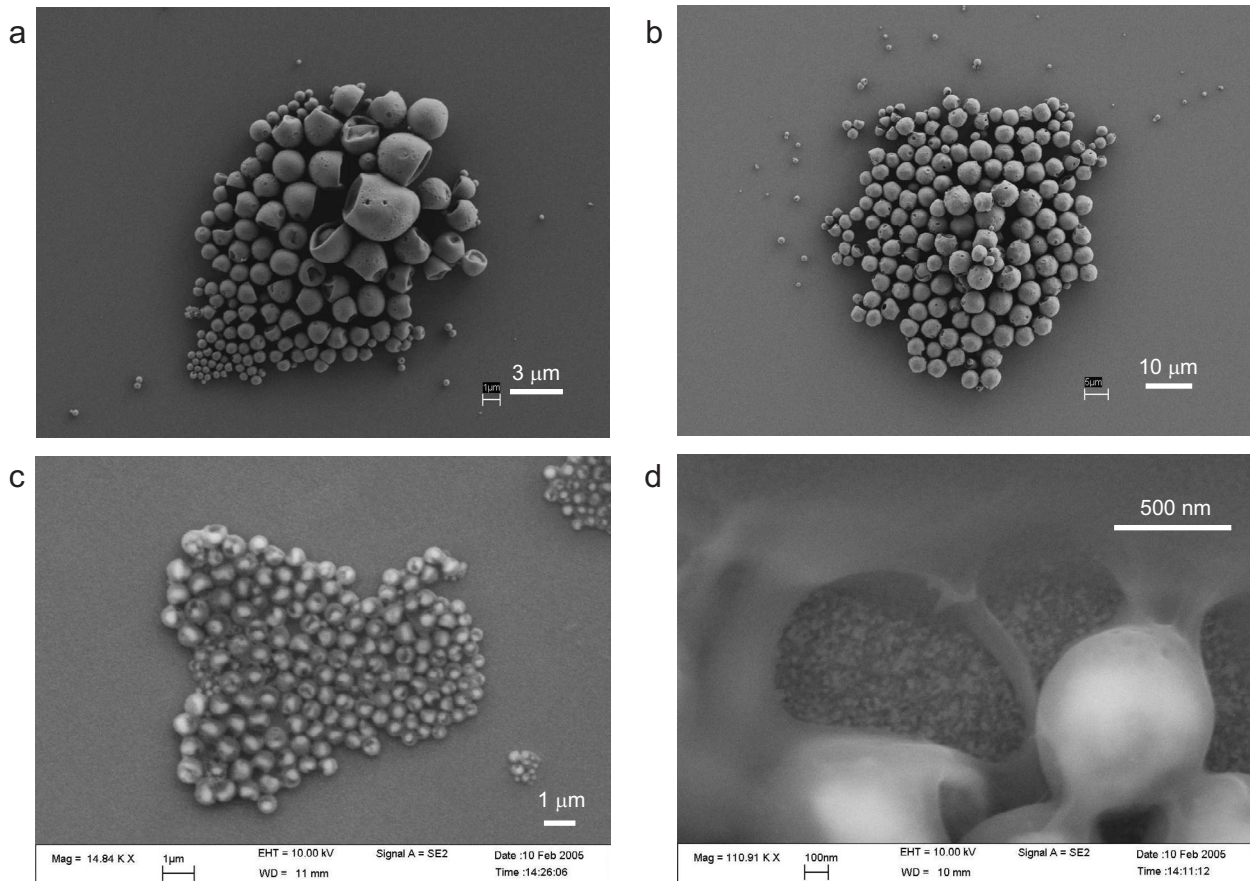


Figure 3.2: SEM images of the micro- and nanobeads. (a) The beads, as received from Merck-Estapor, had an average size of $2.5 \mu\text{m}$ and a wide size distribution. Size selection by centrifugation yielded (b) a batch of microbeads ($4 \mu\text{m}$) and (c) a batch of nanobeads ($0.5 \mu\text{m}$). The nanobeads were imaged without gold-coating on the beads, making the ferrite core visible (d). A thin film of detergent is also seen to remain in the dried-up bead solutions. This had been added by the supplier to prevent aggregation of the beads.

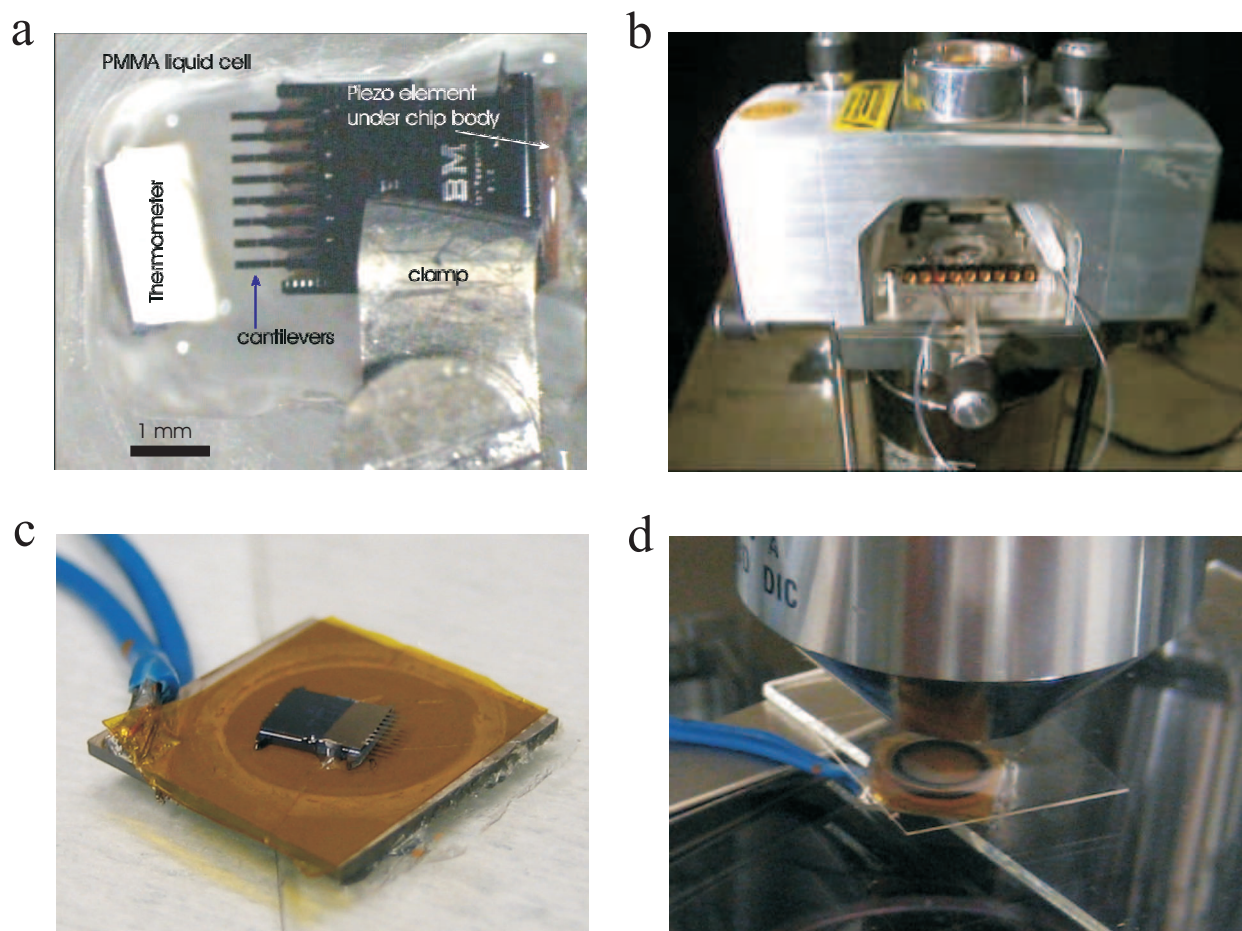


Figure 3.3: The microfluidic cells that contained the microcantilevers. (a) 100- μL PMMA cell closed by an O-ring and a glass cover slide. The cell is 3 mm deep, and the cantilevers are located 1 mm from the bottom. (b) The cell could be placed inside a Nanoscope III head to measure resonance frequencies. (c) 20- μL cell formed simply by an O-ring on top of a piezoelectric actuator. The cover slide is held by capillary forces. The O-ring is 1 mm thick. (d) Either cell could be placed under a microscope to record movements of beads. Shown is the 20- μL cell.

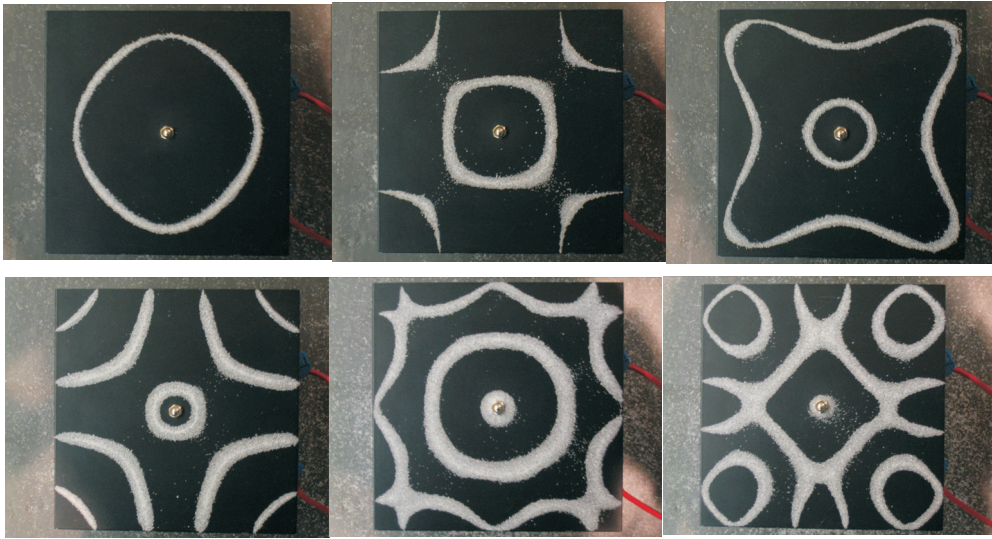


Figure 3.4: Consecutively observed Chladni figures using rough salt grains. The excitation frequencies of the first and last patterns were 0.45 kHz and 6.5 kHz, respectively.

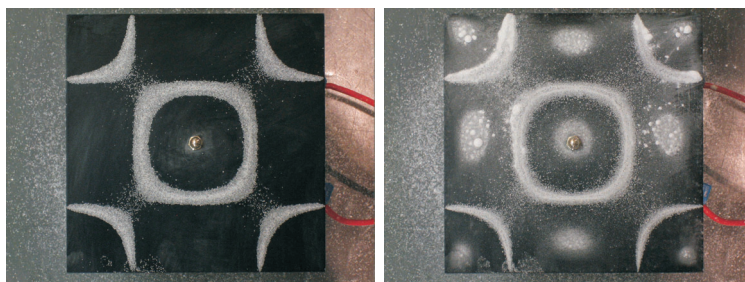


Figure 3.5: Chladni figure with course salt grains (left). When powder sugar was added, an additional patterns was generated on the antinodes (right).

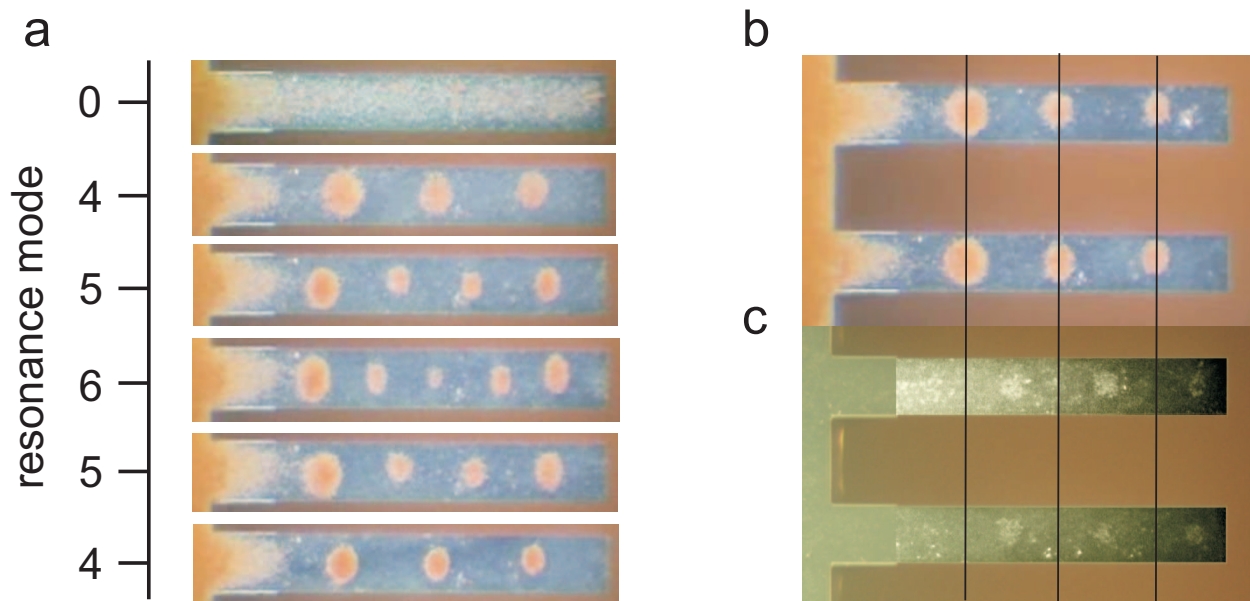


Figure 3.6: (a) Time evolution of microbead patterns on one cantilever (length $560 \mu\text{m}$) upon sequential excitation of different resonance modes (no excitation, 4th, 5th, 6th, 5th, and 4th mode). The total time lapse was 2 minutes. (b) Patterns formed on two adjacent cantilevers by excitation of the 4th mode. Microbeads ($\varnothing 4 \mu\text{m}$) group on the antinodes, whereas nanobeads ($\varnothing 0.5 \mu\text{m}$) group on the nodes (c). Vertical lines mark the positions of the antinodes.

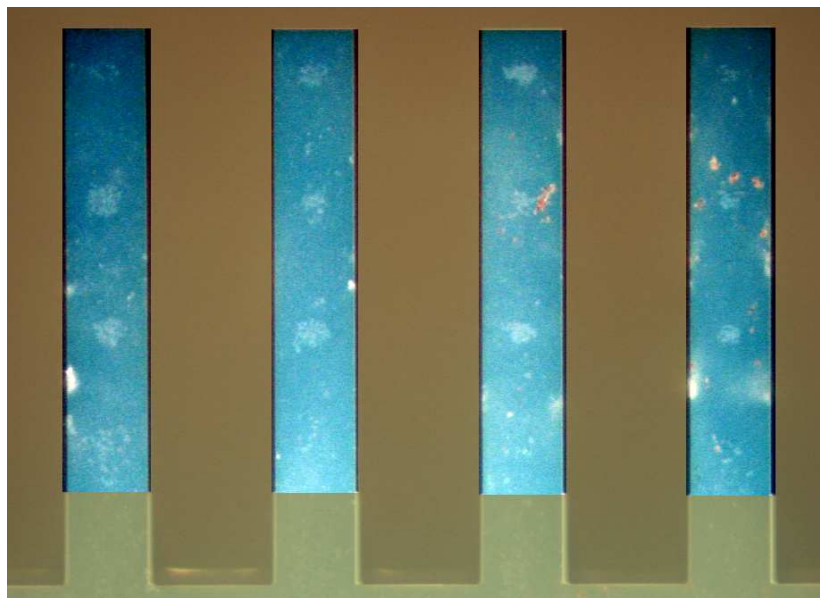


Figure 3.7: Micrograph showing the locations of the antinodes as edge vortices. These are visible due to beads trapped inside the vortices.

drag of boundary streaming towards the antinodes. In microfluidics, both small and large particles follow the direction of boundary streaming, and the particles do not bounce significantly on the oscillating surface. An analytical model of the boundary streaming in water was obtained by solving the Navier–Stokes equation near an infinitely wide, oscillating beam, as published elsewhere [ARG03]. Figure 3.8 shows stream lines of the water near the cantilever surface for the 4th resonance mode. The schematic micro- and nanobeads show how the particle size determines which flow direction of boundary streaming will be followed. The flattened vortices (of cross-section $2 \times 80 \mu\text{m}^2$) are called the inner circulations. The forces on the beads were calculated by integrating the Stokes drag force over the height of the sphere, using

$$F_D = 3\pi\eta \int_0^D u(h)dh,$$

where u is the horizontal component of the water velocity, h is the distance from the cantilever surface, D is the bead diameter, and η the viscosity.⁸ A critical bead diameter was thus obtained that depends on the height of the inner circulations. This height is frequency-dependent, and the resulting graph is shown in Fig. 3.9. A fit was made using the simple formula for the Stokes boundary layer thickness δ . From the figure it can be seen that the nanobeads were smaller than the critical bead diameter in the entire frequency range, whereas the microbeads were larger than the critical size above 100 kHz. In sorting applications, smaller critical sizes would be required for separating sub-micrometer scale objects. This is achieved at higher frequencies while controlling the node-node distance by the choice of the beam thickness.

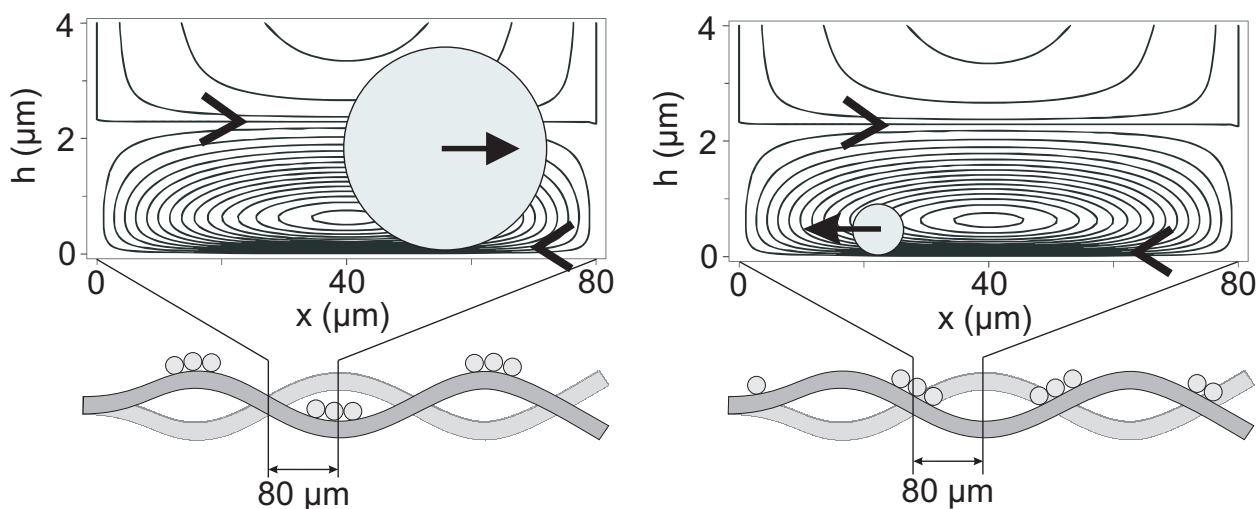


Figure 3.8: Calculated stream lines for water near the surface of an oscillating microcantilever. Shown is the 4th resonance mode, for which the quarter-wavelength was $80 \mu\text{m}$ and the frequency 500 kHz. The cantilever was modeled as being infinitely wide and long. The x -axis coincides with the cantilever axis, and the h -axis extends into the bulk liquid. Differently sized beads are dragged in opposite directions.

The beads interacted with the cantilever surface by weak forces. Two observations suggest that while grouping on the oscillating surface, the microbeads bounced slightly, whereas the nanobeads rolled or hopped intermittently. During intermittent hopping, beads remain bound to the surface until released by thermal energy. Before resorbing, they migrate in the direction of the streaming

⁸Note that for uniform velocity u , the conventional Stokes formula results.

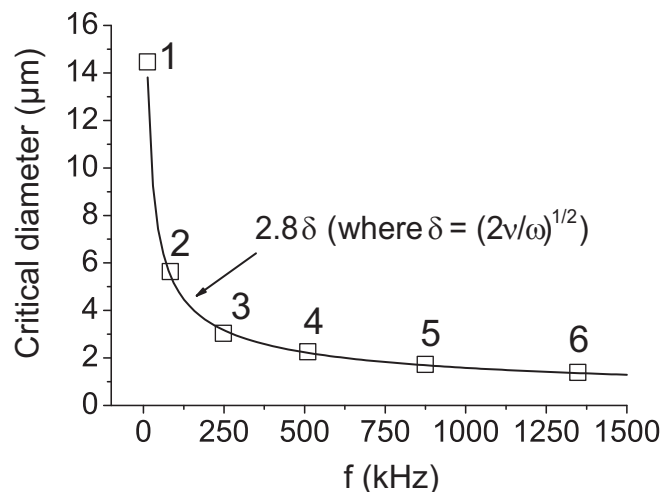


Figure 3.9: Critical bead diameter vs. frequency, which indicates the critical size for particle sorting (squares). The horizontal force of boundary streaming acting on a spherical particle was calculated from the integrated Stokes drag force. The continuous line corresponds to the Stokes boundary layer thickness δ multiplied by a fit factor of 2.8, where ω is the radial frequency of oscillation and ν the kinematic viscosity of the medium.

flow. The first observation is that the nanobeads followed the narrow stream closest to the surface. This indicates that they were held close to the surface, whereas the simple Boltzmann height distribution predicts an average nanobead height $\langle h \rangle$ of $9 \mu\text{m}$ from

$$\frac{n}{n_o} = \exp\left(-\frac{m^*gh}{kT}\right) \Rightarrow \langle h \rangle = kT/(m^*g),$$

where k is Boltzmann's constant, T the temperature, m^* the buoyant mass⁹ of a bead, and g the acceleration due to gravity. The second observation is that the $0.5\text{-}\mu\text{m}$ nanobeads moved 30–50 times slower along the cantilever surface than the $4\text{-}\mu\text{m}$ microbeads did. This suggests that the nanobeads were slowed down by interaction with the surface. For the $4\text{-}\mu\text{m}$ microbeads, on the other hand, the surface interactions were conceivably dominated by the vertical momentum of the beads. The surface transferred a 500-times larger kinetic energy to the microbeads than to the nanobeads, owing to the difference in their mass. The propagation velocity of the nanobeads might be enhanced by tuning the surface chemistry with appropriate buffering of the environmental solution. The chemical interaction can be tuned by adapting the chemical groups [Heg00, Her96] and controlling the pH.

For completeness, the relevant forces acting on the beads are now discussed in detail (see Fig. 3.10). Firstly, the beads possessed kinetic energy due to cantilever oscillation. The velocity amplitude of the cantilever was 63 mm/s for the 4th mode (500 kHz at an amplitude of 20 nm). The masses of the nanobeads ($0.5 \mu\text{m}$) and microbeads ($4 \mu\text{m}$) were 0.11 pg and 57 pg , respectively. Assuming sinusoidal vertical motion, this corresponds to kinetic energies of 53 kT and $27 \times 10^3 \text{ kT}$ and acceleration forces of 22 pN and $11 \times 10^3 \text{ pN}$. The weights of the beads are much smaller: 1.1 fN and 560 fN , or, when accounting for buoyancy, 0.4 fN and 230 fN . If there were no physiochemical interaction between the beads and the surface, the beads would “bounce” up to respective heights of 1.5 and 90 nm (time constant τ being 24 ns and 1500 ns), for the nano- and microbeads

⁹The density of the medium is subtracted from the density of the beads.

(again 4th mode). This was calculated using the Stokes drag force $F(t) = -3\pi\eta D\dot{h}(t)$, η being the viscosity and D the bead diameter. Solving the equation of motion $F(t) = m\ddot{h}(t)$ using the boundary conditions $h(0) = 0$ and $\dot{h}(0) = 2\pi f A$ (where $f = 500\text{kHz}$, $A = 20\text{nm}$, $m = \rho\frac{\pi}{6}D^3$, $\rho = 1700\text{kg/m}^3$) yields for the bouncing height

$$h(t) = \frac{\pi\rho}{9\eta}fAD^2(1 - \exp(-t/\tau)),$$

where the time constant $\tau = \rho D^2/18\eta$.

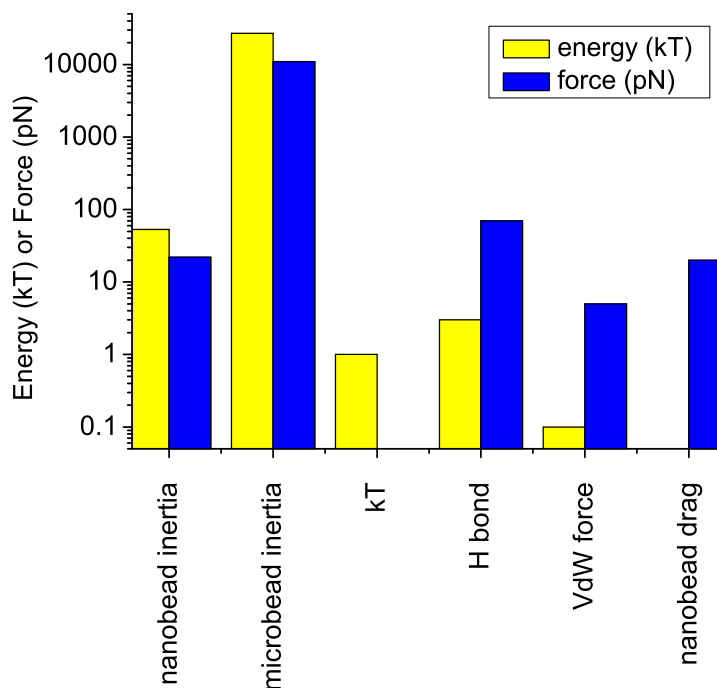


Figure 3.10: Summary of the main forces acting on a bead, and their associated energies. “Nanobead inertia” and “microbead inertia” indicate vertical acceleration from the motion of the cantilever. “kT” is the thermal energy, “H bond” stands for a low-energy hydrogen bond (N–H · · O), and “VdW force” is short for the Van der Waals force between an oxygen and a hydrogen atom. “Nanobead drag” indicates the horizontal drag force from boundary streaming midway between a node and an antinode.

Secondly, the beads were driven by thermal energy. According to the earlier mentioned Boltzmann height distribution, the mean heights above the cantilever surface would be $9\ \mu\text{m}$ and $17\ \text{nm}$ for the nano- and microbeads, respectively. These heights are large compared to the theoretical bouncing heights.

Thirdly, the beads interacted with the surface via weak bonds. The beads were thiol (-SH) functionalized and the cantilever surface consisted of SiO_2 .¹⁰ On the SiO_2 surface, most O atoms are bound to two Si atoms (the singly-bound O atoms present themselves as OH groups). It is not

¹⁰Here we neglect the influence of any oil molecules physisorbed on the surface. In addition, there might have been some photoresist left on the surface from fabrication. Cantilevers were only cleaned in a stream of ethanol, without piranha cleaning. The photoresist was of the Novolac type (partially cross-linked phenol moieties), which contains -OH groups but is otherwise hydrophobic.

known to the author whether hydrogen bonds can form between SH groups on the bead and the O atoms on the surface. Discussions with chemists lead to the conclusion that if such a hydrogen bond exists, it is a relatively weak one due to the size of the sulfur atom. The energies of the classical hydrogen bonds range from 8 kJ/mol for N–H ··· O to 29 kJ/mol for O–H ··· N [wik]. So the bond energy for S–H ··· O is less than 8 kJ/mol, i.e. less than 3 kT. The force required to break the bond is estimated from the typical bond length in water of 0.20 nm [wik] and assuming a linear increase in potential energy with distance. Thus, $F = (8 \text{ kJ/mol}) / N_A / L_b = 70 \text{ pN}$, where N_A is Avogadro's number (6.0×10^{23}) and L_b the bond length. The minimum value for the interaction energy is that given by the Lennard-Jones potential (of which the attractive term describes the Van der Waals force):

$$V(r) = \frac{\gamma_{12}}{r^{12}} - \frac{\gamma_6}{r^6}$$

where r is the distance between the atoms in Å. For H and O atoms, $\gamma_{12} = 4.17 \times 10^{-17} \text{ J} \cdot \text{Å}^{12}$ and $\gamma_6 = 2.71 \times 10^{-19} \text{ J} \cdot \text{Å}^6$ [Med], giving a binding energy of $0.4 \times 10^{-21} \text{ J}$, or 0.2 kJ/mol, or 0.1 kT. The corresponding maximum force is obtained from $F = -dV/dr$ and is 5 pN. So the interaction force between bead and surface is 5–70 pN times the number of involved bonds.

Fourthly, the beads were dragged along the cantilever surface by the boundary streaming. The horizontal drag force was calculated using the adapted Stokes formula shown earlier. The velocity $u(h)$ was evaluated midway between a node and an antinode; the resulting force is plotted in Fig. 3.11. For the 4th mode, we see that the drag force on the 0.5- μm nanobead is only 1 pN per nm of cantilever amplitude, or 20 pN for the typical 4th-mode amplitude.

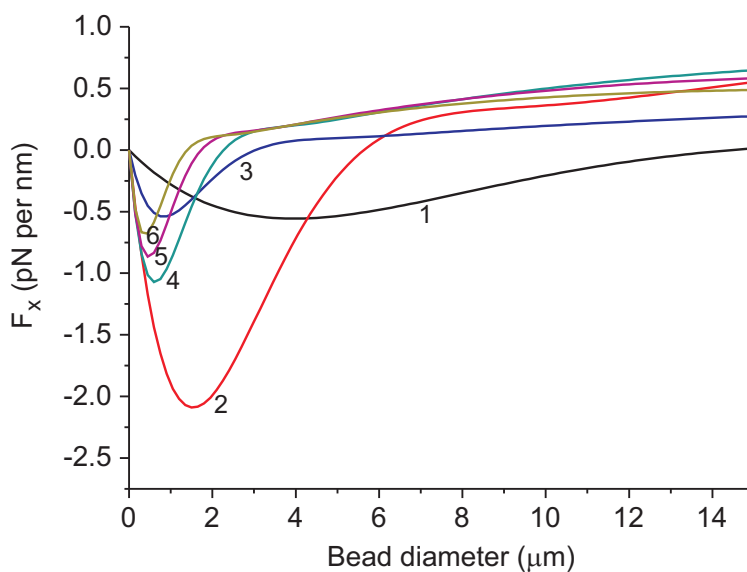


Figure 3.11: Calculated horizontal drag force F_x on a bead of certain diameter. The considered bead is located on the cantilever surface, midway between a node and an antinode. Curves labeled 1–6 indicate the six resonance modes. The forces are expressed per nm of the cantilever oscillation amplitude. Typical amplitudes range from 500 down to 7 nm for modes 1–6, respectively.

In conclusion, the kinetic energy of the nanobeads would only have been enough to break 20–500 bonds simultaneously. The microbeads, on the other hand, could break $27 \times 10^3 / 53 \approx 500$ times as many: 10^4 – 10^5 bonds. It is conceivable that the actual number of bonds involved is on the order of 10^3 – 10^4 , thus explaining why the nanobeads appeared to remain at the surface and why the microbeads traveled more than 30 times faster. The remaining question is whether the

nanobeads rolled or hopped along the surface. The drag force on a nanobead of 20 pN from the boundary streaming was only strong enough to break 0–4 bonds simultaneously. However, the drag force could nevertheless roll the bead along the surface. This can be seen as follows. The bonds are continuously fluctuating between a bound and an unbound state.¹¹ Due to the bond fluctuations, bound nanobeads could perform a random walk along the surface. Any horizontal force will then bias this random walk. Analogously, intermittent hopping of nanobeads can be explained. For example, hydrogen bonds typically perform thermal vibrations with GHz to THz frequencies. For every cycle of the vibration, for the highest binding energy considered (3 kT), the chance of crossing this energy barrier is $\exp(-3)$ (according to Boltzmann statistics). This leaves a bond 10^7 – 10^{10} opportunities per second to break. Assuming that up to 10^4 bonds are involved in the binding of one bead, all bonds are expected to have broken at least once in any period of 1 μ s to 1 ms. When this period is typically too short for a single pair of atoms to find each other again, the entire bead is free. Based on this simple calculation, intermittent hopping is expected to take place when relatively few bonds are involved in the bead-surface interaction.¹²

The cantilever amplitudes for different resonance modes can be obtained by multiplying the data in Fig. 3.12 by the typical drive voltage of 10 V_{pp}. The linear fit of ($A \sim 1/f^{1.5}$) matches with theory, which can be seen as follows. $A(f_n) = Q(f_n)F/k(f_n)$, where f_n is the frequency of the n th resonance mode, $Q(f_n)$ the quality factor, F the driving force, and $k(f_n)$ the spring constant [Sad05]. $Q(f_n) \sim \sqrt{f_n}$, since for $Re \gg 1$, $Q(f) \sim \sqrt{Re(f)}$ [SLM95], where $Re(f) \sim f$, Re being the Reynolds number. $k(f_n) \sim f_n^2$, because [CMS00] $k(f_n) = m_e(2\pi f_{vac,1})^2$, where $f_{vac,1}$ is the fundamental frequency in vacuum and the effective mass $m_e = 0.2427m$ accounts for the fact that the cantilever's mass m is not concentrated at its free end. Furthermore, $f_{vac,n}/f_{vac,1} = C_n^2/C_1^2$, where C_n is the n th positive root of $1 + \cos C_n \cosh C_n = 0$. Finally, $f_{vac,n}/f_{water,n}$ is, for the cantilevers described here, by good approximation independent of frequency (n being the mode number): according to Inaba *et al* [IAM93], $f_{vac,n}/f_{water,n} = \sqrt{1 + \alpha(f) + \beta}$ where (for the here described system) $\alpha(f) \approx 0.002\beta$, the “reactance term” β depending only on geometrical factors and mass densities. So

$$A(f_n) = Q(f_n)F/k(f_n) \sim \sqrt{f_n}/f_n^2,$$

and therefore $A(f) \sim 1/f^{1.5}$. The deviation of the first mode from this trend is in part due to the fact that its mode shape does not approximate a sinusoidal shape; instead, a relatively large edge vortex is generated around the end of the cantilever, which dissipates energy, thus lowering the amplitude. In addition, in the calculation above the stated f -dependency of A is only valid for $Re \gg 1$; the influence of f is reduced for lower f values. Both mechanisms contribute to the “reduced” amplitude of the first mode.

¹¹This is due to thermal energy and competitive binding by water molecules.

¹²Also, lower binding energies and higher thermal vibration frequencies would favor intermittent hopping, but this combination is contradictory from a mechanical point of view.

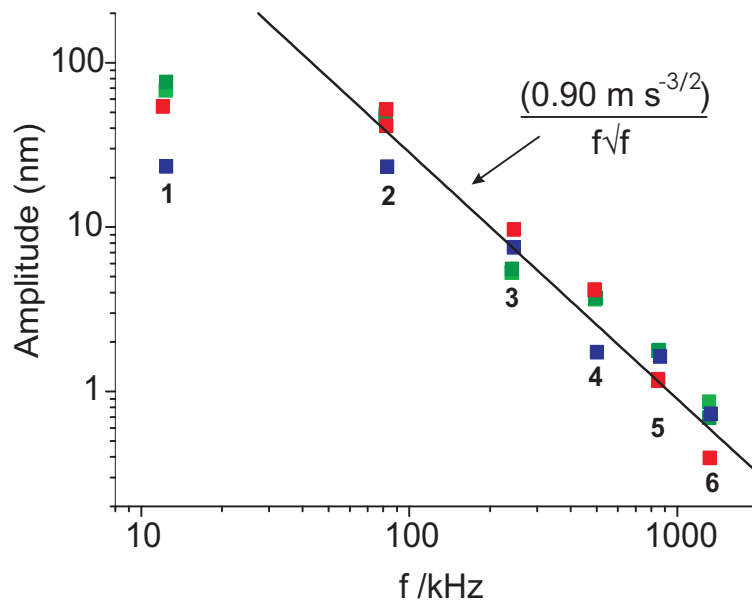


Figure 3.12: Measured cantilever amplitudes for a piezo drive voltage of $1 V_{pp}$, at the frequencies of the first six resonance modes. All experiments were performed with the same cantilever array, except the blue data points. Temperature variations did not have a significant influence on the results: the light- and dark-green data points were recorded at 28°C and 35°C , respectively. The linear fit of $(A \sim 1/f^{1.5})$ matches with theory.

3.3 The physics of boundary streaming near an oscillating surface

Acoustic streaming is steady streaming observed in gases and liquids when these are excited by an oscillatory force. It is known to occur in three situations: in the bulk medium by action of a sound field, close to an obstacle onto which a sound field impinges, and close to an oscillating surface (“boundary streaming”). Especially the boundary streaming type is relevant for recently introduced MEMS and NEMS devices: apart from dynamic-mode AFM and cantilever sensors, there are microfluidic mixers [SDA02] and biosensors based on surface acoustic waves (SAW) and flexural plate waves (FPW).

As early as 1884, boundary streaming was mathematically described by Lord Rayleigh [Ray84]. The velocity field was obtained by solving the Navier-Stokes equation for an oscillating boundary. In 2003, Açıkalın *et al* obtained a velocity field in a similar manner for oscillating plane surfaces, including cantilevers [ARG03]. However, this method does not provide insight into the physics of the phenomenon.

This work presents a detailed description of the physics of boundary streaming. Simple physical analogies are used to arrive at a streaming pattern that is similar to the solution by Açıkalın *et al*. It starts with the simple first-order velocity field that follows from the periodic motion of the surface. The physics is then explained in three steps. Firstly, when the first-order velocity field is regarded in the reference frame of the moving cantilever, it may be approximated by the simple model of fluid impinging onto a flat surface. Secondly, the no-slip condition is forced by comparison to the second Stokes problem. The resulting vorticity in the flow field causes the nonlinear inertia force to have a nonzero time-average. Thirdly, from this force field follows the streaming pattern by modeling individual streams as straight channels and integrating the force. The dimensions and velocities of the resulting vortices correspond to the known mathematical solution.

First-order solution

A planar surface is modeled, which is oscillating in an infinite fluid medium. Numerical parameters are chosen as to resemble an oscillating cantilever in water. The cantilever’s frequency and wavelength match those of the type used in section 3.2. The oscillation is driven in the fourth flexural resonance mode. The model neglects “edge effects”, i.e. the flows near the cantilever’s edges; the cantilever is considered to be infinitely wide and long. The wave vectors of the standing wave are chosen along the x axis. The resulting first-order oscillatory motion of the liquid may best be imagined as described by Weigert, Dreier, and Hegner in 1996 [WDH96], see Fig. 3.13. In this model, cylinder-shaped volumes of water rotate back and forth around the nodal lines. Within the cylinders, the viscous shear forces are negligible; they rotate one-to-one with the surface. This will be used below to simplify the first-order calculation.

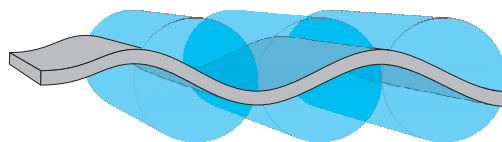


Figure 3.13: Scheme of an oscillating membrane in liquid, as suggested by Weigert, Dreier, and Hegner. The blue areas represent the cylinder-shaped water volumes that rotate with the surface around the nodal lines.

To calculate the velocity field, the Navier-Stokes equation for incompressible fluids is used.¹³ This equation of motion equates the acceleration of a fluid element's mass to all forces acting on it:

$$\rho \frac{D\vec{v}}{Dt} = -\nabla p + \mu \nabla^2 \vec{v} \quad (3.1)$$

where ρ is the density, μ the dynamic viscosity, p the local pressure, and \vec{v} the local velocity. For a first-order solution, $D\vec{v}/Dt \approx \partial\vec{v}/\partial t$ may be used (see next section). The external-force term can be removed, since gravity can be neglected and the forces from the moving boundary will be accounted for in the pressure term. The viscous term may also be neglected, as mentioned earlier. Then,

$$\rho \frac{\partial\vec{v}}{\partial t} = -\nabla p. \quad (3.2)$$

The pressure p results only from the surface oscillation (wave number k_{wave}), and it is known to fall off exponentially into the bulk liquid (decay constant k_{decay}). Therefore, it is of the form

$$p = P \sin(k_{\text{wave}}x) \exp(-k_{\text{decay}}y) \cos(\omega t). \quad (3.3)$$

Because the liquid is incompressible, the pressure distribution must obey the Poisson relation

$$\nabla^2 p = 0. \quad (3.4)$$

Substitution of Eq. 3.3 into Eq. 3.4 gives

$$k_{\text{decay}} = k_{\text{wave}} \equiv k.$$

Now \vec{v} can be solved from Eq. 3.2 to give

$$\vec{v} = \begin{pmatrix} -V \cos(kx) \exp(-ky) \sin(\omega t) \\ V \sin(kx) \exp(-ky) \sin(\omega t) \end{pmatrix} \quad (3.5)$$

$$V = \frac{Pk}{\omega\rho}, \quad (3.6)$$

which is plotted in Fig. 3.14(a). The parameter values are those of the microscale Chladni figure experiments (4th resonance mode, see Section 3.2): $\omega = 2\pi \cdot 500$ kHz, $k = 2\pi/(200 \mu\text{m})$,¹⁴ $\rho = 1000$ kg/m³, and $P = 6.3$ kPa. Here, P was determined using the measured cantilever amplitude $A = 20$ nm (from the time-integrated velocity, it can be seen that $A = Pk/(\omega^2\rho)$).

New frame of reference

The bottom of the water bath oscillates, so we have a moving boundary of the system. We will look at the water flow *with respect to this moving boundary*. So we will let our coordinate system follow the motion of the surface. This is done by subtracting the velocity of the boundary from the entire velocity field. The result is shown in Fig. 3.14(b); liquid impinges onto the upward-moving antinodes.

¹³For the system under consideration, even gases may be regarded as being incompressible, as long as $\omega L \ll c$, where c is the speed of sound, ω the angular frequency, and L the node-node distance [Tel81].

¹⁴The experimental node-node distance is about 100 μm .

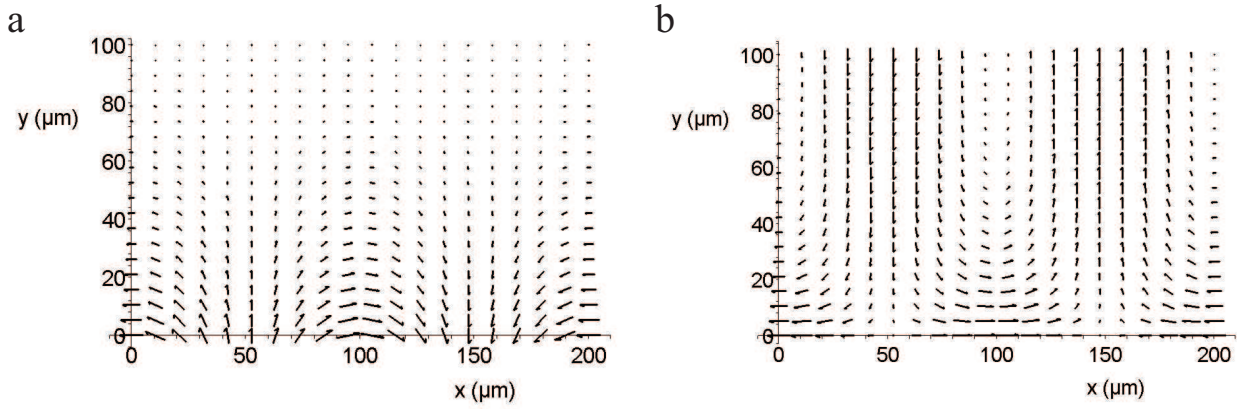


Figure 3.14: Vector field of the water velocity in the first-order solution at $t = T/4$, T being the period. The longest arrows represent 6 cm/s. In the static reference frame (a), the upper halves of the cylinder-shaped water volumes of Fig. 3.13 can be recognized. In the reference frame of the moving surface (b), the flow is seen to impinge onto the upward-moving antinode.

The problem of liquid impinging onto a surface is well-known in fluid dynamics. The classical solution for such a velocity field is:

$$\vec{v} = (Cx, -Cy). \quad (3.7)$$

Close to the stagnation points, this solution matches our vector field (Fig. 3.14(b)). The constant C is found to be $2.0 \times 10^3 \text{s}^{-1}$, which will be used in the next section. The velocity field of (3.7), however, is too inaccurate an approximation for the entire field and will not be used further.

No-slip condition

Note that the no-slip condition is violated: there is a tangential velocity at the surface. This is not surprising, because this condition was not applied yet. This will be done now. The no-slip condition was added in 1911 by Hiemenz [Hie11]. The differential equation he used does not have an analytical solution [Bat94]. His numeric result is shown in Fig. 3.15, along with a function that approximates it. This indicates that the following correction to the velocity component v_x would be a good approximation for forcing the no-slip condition:

$$v_{x, \text{ no slip}} = v_{x, \text{ slip}} \times (1 - \exp(-1.5y/\delta)). \quad (3.8)$$

For the boundary layer thickness δ , there are two definitions. The first defines it as the distance at which the velocity reaches 99% of the bulk velocity. However, for impinging liquid, the bulk velocity is not defined. Then the second definition becomes more convenient: δ is defined as the distance from the surface where the inertia and viscous forces are comparable (i.e. where the Reynolds number $\text{Re} = 1$).¹⁵ Here,

$$F_{\text{viscous}} = |\mu \nabla^2 \vec{v}| / \rho \approx \frac{\mu Cx}{\rho \delta^2} \quad (3.9)$$

¹⁵The most popular definition of the Reynolds number is $\text{Re} = \rho v D / \mu$. However, this is only valid for flow through a pipe of diameter D . For arbitrary systems, D and v are not well-defined. Another definition states that $\text{Re} = F_{\text{inertia}} / F_{\text{viscous}}$, where $F_{\text{inertia}} = |\vec{v} \cdot \nabla \vec{v}|$. So the linear inertia term $\rho \partial v / \partial t$ is either neglected or just not part of the definition. The author has chosen to stay with the definition.

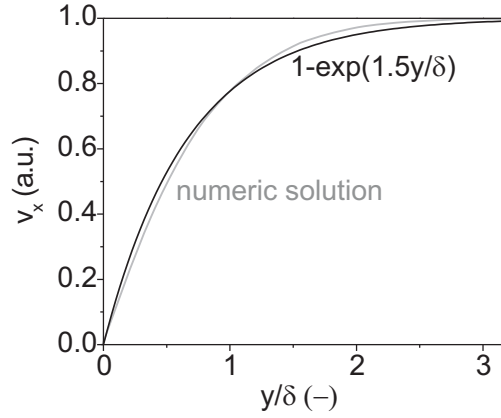


Figure 3.15: Velocity profile in the boundary layer near a stagnation point. The numeric solution by Hiemenz (1911) (grey) is shown along with an exponential function fitted by eye (black). The horizontal axis is scaled relative to the boundary layer thickness δ .

$$F_{\text{inertia}} = |\vec{v} \cdot \nabla \vec{v}| \approx C^2 x \quad (3.10)$$

$$F_{\text{viscous}} = F_{\text{inertia}} \Rightarrow \delta \approx \sqrt{\frac{\mu}{\rho C}} = 22 \mu\text{m}, \quad (3.11)$$

where F denotes force per unit mass, and μ is 1.0 mPa·s for water of 20°C. The expression for F_{inertia} is derived in Section 3.3.

This *would* describe the boundary layer well if the flow were *stationary*. However, the considered flow is oscillatory. This situation is reminiscent of the so-called second Stokes problem [SG00]. It describes flow near a plate oscillating laterally in its own plane. Stokes showed that the amplitude of the oscillatory motion of the fluid dies out exponentially into the bulk fluid. The layer within the “1/e distance” is called the Stokes boundary layer. Its thickness is

$$\delta_{\text{Stokes}} = \sqrt{\frac{2\eta}{\rho\omega}} = 0.8 \mu\text{m}.$$

Turning the second Stokes problem around, the bulk fluid is oscillating back and forth over a steady surface. The fluid can communicate its oscillation over maximally a distance dictated by the Stokes boundary layer thickness. This is illustrated in Fig. 3.16. Therefore, the velocity profile corrected for the no-slip condition should be

$$v_{x, \text{ no slip}} = v_{x, \text{ slip}} \times (1 - \exp(-y/\delta_{\text{Stokes}})), \quad (3.12)$$

using which the v_x velocity is plotted in Fig. 3.17.

The driving force

$D\vec{v}/Dt$ stands for the acceleration of a fluid element *in the reference frame of the moving element*. This is generally not equal to $\partial\vec{v}/\partial t$, which is defined at a fixed point in space and is called the *local* rate of change. We will see below that the following correction is required:

$$\frac{D}{Dt} \equiv \frac{\partial}{\partial t} + \vec{v} \cdot \nabla.$$

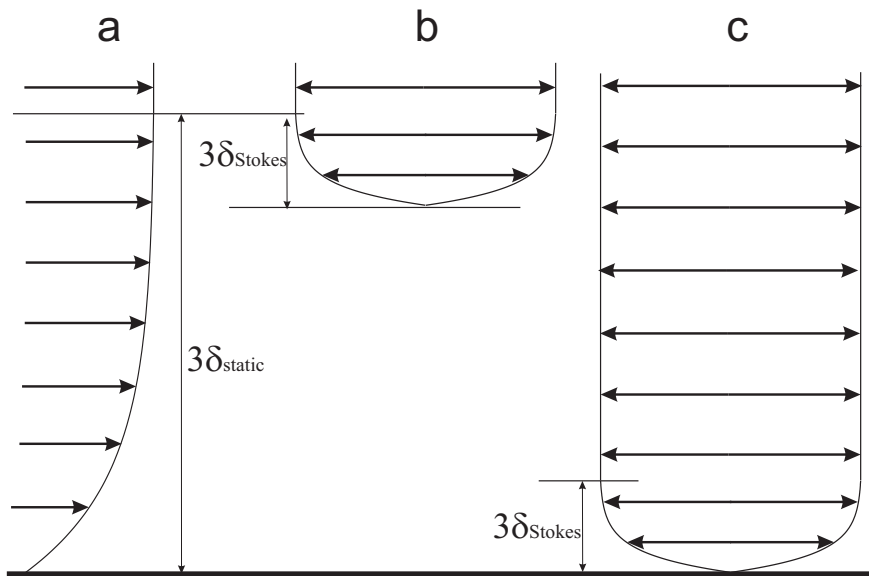


Figure 3.16: Choice of the boundary layer thickness. (a) The steady-flow boundary layer. (b) An oscillating bulk fluid can only communicate its oscillation as far as several times δ_{Stokes} into a neighboring body of fluid. The drawn case is of course not realistic; the system would equilibrate to situation (c).

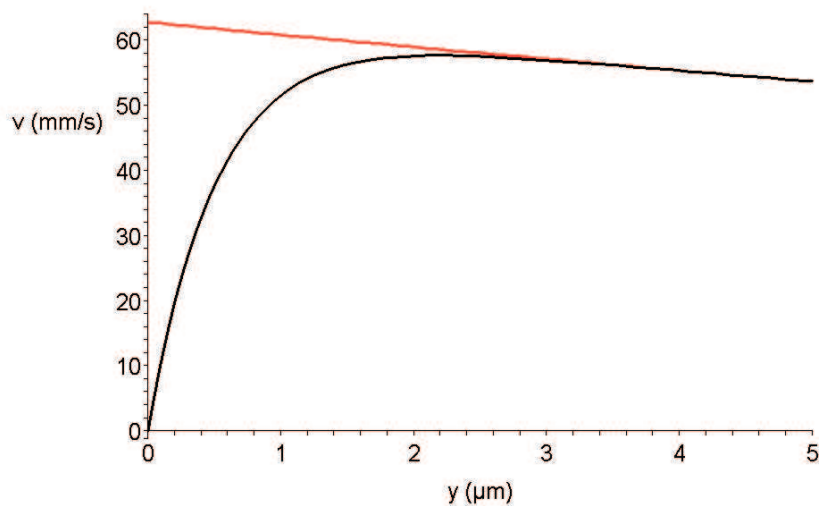


Figure 3.17: The v_x component with slipping boundary (red) and corrected (black) using the Stokes boundary layer thickness.

It is the second term on the right-hand side that causes the boundary streaming, which will be shown later. It is called the *convective* rate of change in momentum. Because of its importance, the expression will now be derived using an example. Suppose you are on a boat tour in the wilderness of Venezuela. You are on a wide and fast-streaming river and you fear that you might be approaching a waterfall. Knowing that water accelerates close to a waterfall, you decide to measure the local $\partial v/\partial t$. You throw out an anchor, put your hand in the water, and measure $\partial v/\partial t = 0$, as shown in Fig. 3.18. You even make a second measurement 100 m down-stream. Again, $\partial v/\partial t = 0$. However, concluding that the water is not accelerating could be dangerous. The acceleration Dv/Dt of a water element should be measured in the reference frame of this element. In the example, the *absolute* velocities should have been measured at the two positions. Then, assuming constant acceleration,

$$\begin{aligned} \frac{Dv}{Dt} &= \frac{v_2 - v_1}{\Delta t_{\text{flow}}} \\ \Delta t_{\text{flow}} &= \frac{\Delta x}{\langle v \rangle} \\ \Rightarrow \frac{Dv}{Dt} &= \langle v \rangle \frac{v_2 - v_1}{\Delta x} = v \nabla v, \end{aligned} \tag{3.13}$$

where $\Delta x = 100$ m and $\langle v \rangle = (v_1 + v_2)/2$ is the time-averaged velocity. In the last expression, we recognize the mentioned *convective* rate of change.

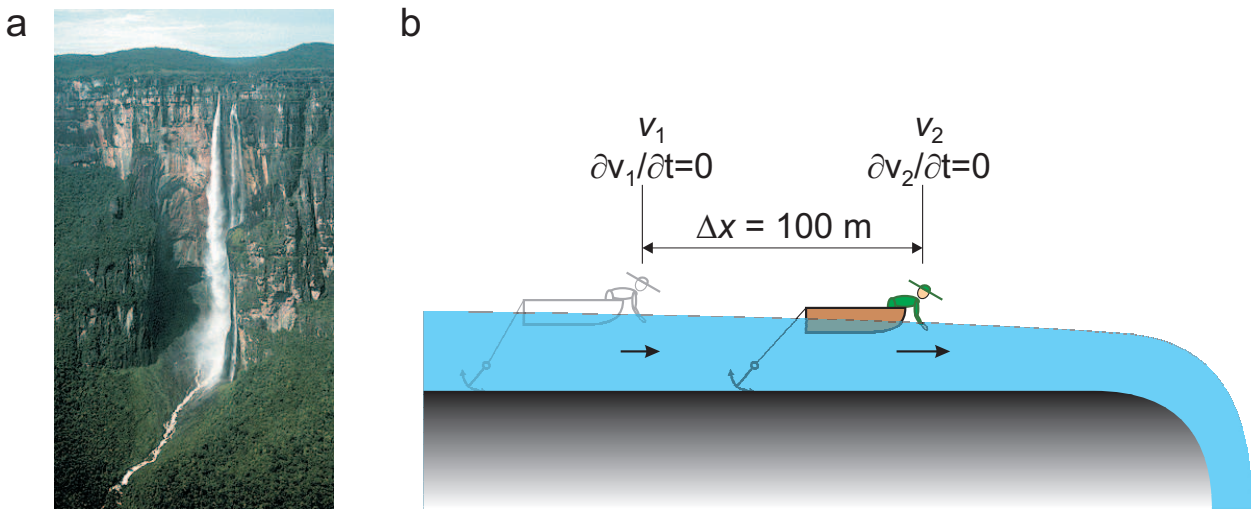


Figure 3.18: (a) Angel Falls, Venezuela. (b) Measurements for predicting the proximity of a waterfall. The acceleration of the flow can be estimated from v_1 , v_2 , and Δx .

The Navier-Stokes equation (3.1) now looks like

$$\rho \left(\frac{\partial \vec{v}}{\partial t} + (\vec{v} \cdot \nabla) \vec{v} \right) = -\nabla p + \mu \nabla^2 \vec{v} \tag{3.14}$$

$$\vec{F}_{\text{inertia1}} + \vec{F}_{\text{inertia2}} = -\nabla p + \vec{F}_{\text{viscous}}. \tag{3.15}$$

All forces have time-average zero, except for $\vec{F}_{\text{inertia2}}$. Its x -component will be found to be the driving force behind boundary streaming. Substituting the \vec{v} from Fig. 3.14(b), corrected for

“no-slip”, it takes the form

$$F_{x,\text{inertia}2} = \rho V^2 \sin(\omega t)^2 f(x, y, k, \delta_{\text{Stokes}}) \quad (3.16)$$

$$\Rightarrow \langle F_{x,\text{inertia}2} \rangle = \rho V^2 f(x, y, k, \delta_{\text{Stokes}})/2, \quad (3.17)$$

where $\langle \cdot \rangle$ indicates a time-average. This force is plotted in Fig. 3.19.

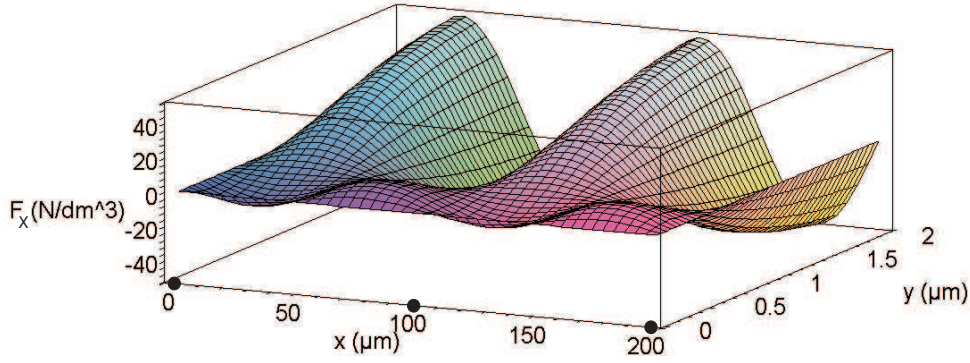


Figure 3.19: The x -component of the time-averaged nonlinear viscosity term, $\langle F_{x,\text{inertia}2} \rangle$. This drives the boundary streaming. Black dots indicate the positions of the nodes of oscillation.

Velocity field deduced from force field

To obtain a velocity field from the time-averaged force field, an assumption has to be made about the resulting flow path. In the horizontal-force field (Fig. 3.19), well-defined “pockets” within the Stokes boundary layer indicate branches of the resulting flow field. These branches form the lower halves of the inner circulations.¹⁶ The second pocket from the left (within $x = 50 - 100 \mu\text{m}$ and $y = 0 - 0.5 \mu\text{m}$) will now be modeled as a rectangular channel. This is a valid approximation, since its width-to-height ratio is high (100:1). First, $\langle F_{x,\text{inertia}2} \rangle$ is (space-)averaged over the channel length to obtain $F_{x,\text{channel}}$. Then, the Navier-Stokes equation is solved for v_x using this as a (height-dependent) external force:

$$\rho \frac{Dv_x}{Dt} = F_{x,\text{channel}} + F_{x,\text{viscous}}. \quad (3.18)$$

Because the system is in steady state, and the channel is long,

$$\frac{D\vec{v}}{Dt} = 0. \quad (3.19)$$

Applying the boundary condition $v = 0$ at $y = 0$ and at $y = 0.5 \mu\text{m}$, the velocity profile of Fig. 3.20 is obtained.

It is now assumed that the x -component of the entire velocity field has the following form:

$$v_x = \alpha \sin(2kx) F_{x,\text{channel}},$$

where α is a proportionality constant that sets the maximum velocity in the flow branches near the surface to the maximum velocity of the channel flow of Fig. 3.20.

¹⁶The inner circulations are the vortices closest to the surface. See for example Fig. 3.21(b).

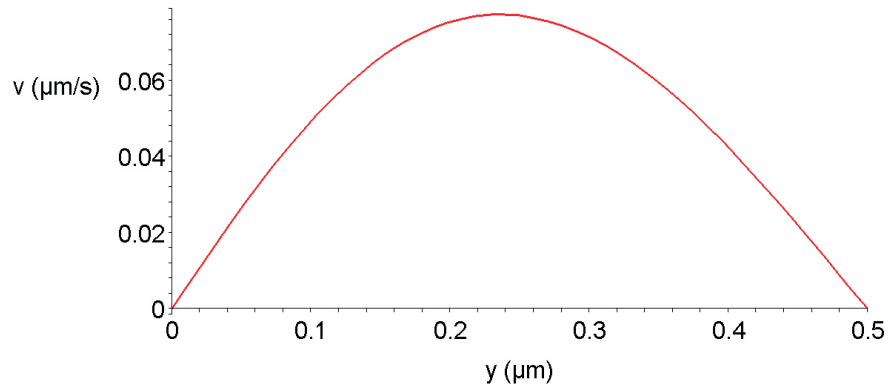


Figure 3.20: The velocity profile in the rectangular channel representing the lower portion of an inner vortex.

The y -component can be solved from v_x using the assumption that the fluid is incompressible:

$$\nabla \cdot \vec{v} = 0$$

The resulting boundary streaming is shown in Fig. 3.21, along with a comparison to the solution by Açıkalın *et al.* The center positions of the vortices are in good agreement, but the velocities differ by three orders of magnitude. One cause is that the Açıkalın solution violates the no-slip condition, allowing unrealistically large velocities near the surface (Fig. 3.21(c)). On the other hand, the here presented model has to some extent underestimated the velocities near the surface: in the rectangular channel, the inlet and outlet pressures were neglected. These contributions may have been significant, since the driving force outside the channel (at larger y -values) was found to be larger than the force inside the channel.

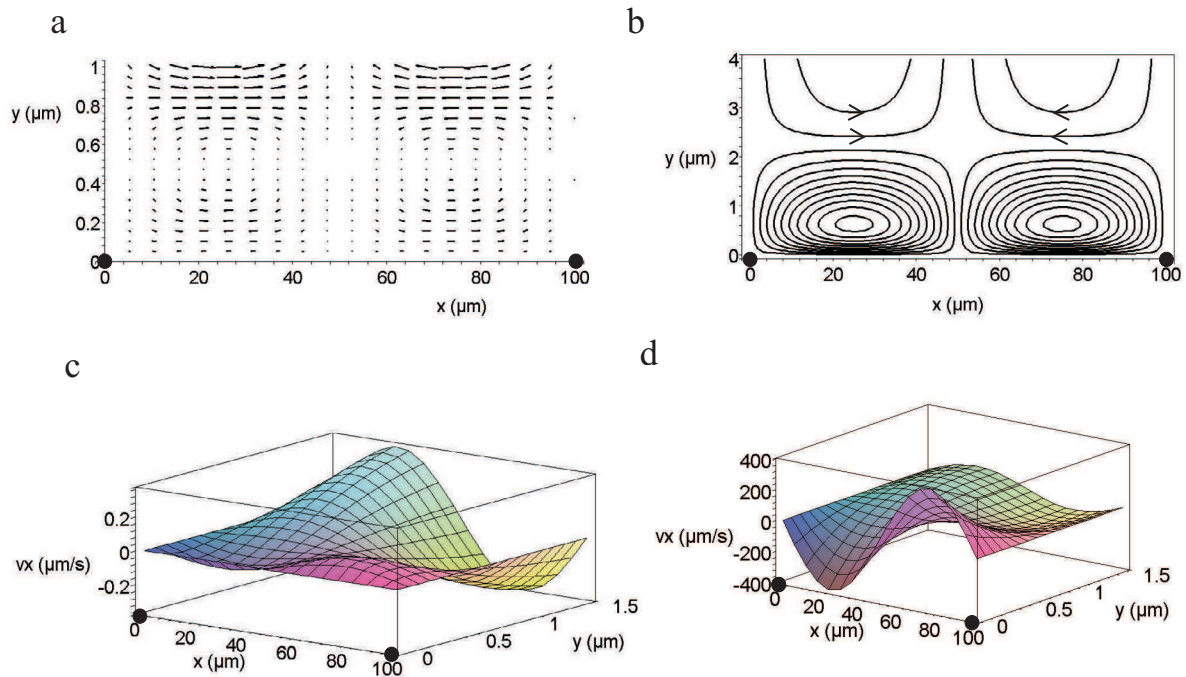


Figure 3.21: Comparison of the results ((a) and (c)) with the solution by Açıkalin *et al*((b) and (d)). Their Maple source code was adapted as to obtain graphs (b) and (d) for our cantilever parameters. The velocity field (a) shows the same vortex center positions as the stream line plot of the Açıkalin solution (b) (centers at $y = 0.5$ and $y = 0.6\mu\text{m}$, respectively). The obtained x -velocities (c) are three orders of magnitude smaller than the Açıkalin solution (d). The latter is also seen to violate the no-slip condition. Black dots indicate the positions of the nodes of oscillation.

Chapter 4

Conclusions and Outlook

The following contributions in the field of nanomechanical sensors in liquid were presented: a novel displacement sensor that can be operated in aqueous solutions and a particle sorting or microfabrication technique based on oscillating cantilevers in liquid. Also, the physics of boundary streaming was clarified for the first time. Combined, these results provide a toolbox for the development of nanomechanical sensors in integrated microfluidic systems.

A novel displacement sensor based on a squeezable molecular multilayer

We developed a novel displacement sensing technique based on the tunneling method and on capacitive detection. The traditional air/vacuum gap between the electrodes was substituted by a squeezable molecular multilayer. Two versions were investigated. For the tunneling method, a setup for proof of concept showed the current vs. distance behavior across a bilayer to be exponential and in the lower nanoampere regime, which resulted in nanometer displacement sensitivity. The main advantages of the tunneling method are inherent vertical alignment of the tunneling electrodes, the ability to operate in aqueous solutions, insensitivity to contamination, low dissipation, and easily detectable tunnel currents. For the capacitive method, a first assessment produced the dielectric constant of a molecular trilayer, which was $\epsilon_r = 1.5$. This is the first time that this type of multilayer has been electrically characterized. The advantages of this version compared to existing capacitive sensors include the prevention of snap-in between the electrodes, and the ability to operate in aqueous solutions. Which of the two versions is the method of choice depends mainly on the range of the displacements. The insulating film can be 1-10 nm thick for tunneling readout, and 1-1000 nm thick for capacitive readout.¹ The down-scalable nature of this sensor offers the possibility of integration into highly parallel sensor arrays. This technique could be a replacement for current technology; it is not only suitable as a readout method for AFM (see figure 4.1), but also for general sensing applications, such as biosensors and magnetic sensors.

Nanomechanical resonators generating Chladni figures and boundary streaming

Inverted Chladni figures were formed on oscillating microcantilevers in the aqueous environment. Microbeads were found to collect on the antinodes, whereas nanobeads moved towards the

¹For films thicker than 50 nm, flexible polymers can be spin-coated.

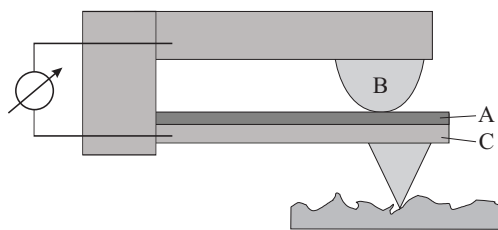


Figure 4.1: Schematic of an application for scanning probe microscopy. Deflection of the cantilever (C) results in compression of the self-assembled bilayer (A). The large-radius tunneling electrode (B) is fixed. The range of deflection could be increased by placing the electrode (B) closer to the support.

nodes of vibration. This demonstrates the inverse size-dependent directionality as compared with Chladni's observations owing to induced streaming of the liquid. The applied analytical model for boundary streaming predicts a critical, frequency-dependent bead diameter at which beads reverse direction, which was experimentally observed. The demonstration of Chladni figures in microfluidics presented here opens the door to highly parallel, directed assembly and to size-based sorting or size-dependent manipulation of particles, organelles, or cells. In sorting applications, particles on the nodes and antinodes could be transported along orthogonal paths such as dielectrophoretic paths [LB02]. Combined with time-segregation, this allows for additional selection on chemical composition of the separated objects. The propagation times can be tuned by the choice of surface chemistry and appropriate buffering of the solution. In patterning applications, the use of membrane structures instead of cantilevers will offer a larger variety of patterns. Grouped particles can be fixed using laser curing, photopolymerization or selective electroless deposition on metal [TP89] or polymer [VGC93]. After fixation, the liquid is removed and the patterns are transferred from the membrane to a chip surface by nanotransfer printing (nTP) [KMD05, HKK04], leading to controlled, multi-step assembly of biotechnological sensors or nanoelectronic circuits.

The physics of boundary streaming

The physics of boundary streaming was clarified for the first time. Successive physical analogies were used to arrive at a velocity field that is similar to a recently published solution of the corresponding Navier-Stokes equation. Although the vortex positions of both solutions matched, the here presented velocities are significantly smaller. These lower values are may be attributable to the the strict adherence to the no-slip condition at the boundary, and should therefore be preferred. A profound understanding of boundary streaming will aid in the development of nanomechanical devices involving oscillatory motion in liquid. These include cantilever biosensors, dynamic mode SPM, and microfluidic mixers.

Outlook

My recommendations for future work are:

- Displacement sensor: microfabrication of the tunneling-based version. When the entire electrodes are coated with the molecular bilayer, the device could be tested in the aqueous environment.

- Displacement sensor: capacitance vs. distance measurements on molecular multilayers or polymer thin-films. A detailed outlook for the development of the capacitive displacement sensor is given at the end of chapter 3.2.
- Chladni figures: fixation of particles to the surface. Groups of metallic or polymer particles could be solidified using electroless deposition, laser curing or photopolymerization.² Biological cells attach by themselves to various coated surfaces.
- Chladni figures: variation of the nanobead-surface interaction. A smaller binding force will expectedly prevent these beads from forming groups on the nodes, due to the Boltzmann height distribution. A larger force should prevent them from moving at all. This could shed light on the suggested mechanisms of propagation.
- Chladni figures: control over the line width of generated patterns. The following parameters could play a role: the particle-surface interaction forces, the particle-particle interaction, and the amplitude of oscillation.
- Chladni figures: alignment of nanotubes or nanowires along the nodal lines of oscillating membranes. This could lead to a cost-effective fabrication method for nanotube-based electronics. Patterns generated on membranes could be transferred to chip surfaces by an adhesive carrier; this technique is compatible with very small particles [KMD05].
- Boundary streaming: mixing of analyte near oscillating cantilevers. The mixing should reduce the time required by cantilever sensor experiments. This could be made visible as follows. A cantilever could be functionalized with the horseradish peroxidase (HRP) enzyme (0.1% in phosphate buffer). HRP catalyzes the conversion of the colorless solution of tetramethylbenzidine (TMB) into a dark blue solution. Without oscillation, it should take longer for an injected TMB solution to turn blue. In addition, when the cantilevers are mounted sideways under the microscope, the boundary streaming might become visible by the blue tracer.

²It this case, polymer particles (e.g. polystyrene) act as the substrate on which polymerization is initiated. The photo initiator for UV radiation is usually a benzoyl chromophor (e.g. benzophenone), which exhibits a good absorption in the UV wavelength range and a good photochemical reactivity. The monomer could be acrylic acid [win05]. Both the initiator and the monomer should have been present in the original bead solution because an additional liquid injection could disturb the bead patterns.

Bibliography

- [AAZ89] S. Akamine, T. R. Albrecht, M. J. Zdeblick, and C. F. Quate. “Microfabricated scanning tunneling microscope.” *IEEE Electron Device Lett.*, **10**:490–492, 1989.
- [ALL03] M. K. Araz, C.-H. Lee, and A. Lal. “Ultrasonic separation in microfluidic capillaries.” In *2003 IEEE Ultrasonics Symposium*, pp. 1066–1069, 2003.
- [ARG03] T. Açıkalin, A. Raman, and S. V. Garimella. “Two-dimensional streaming flows induced by resonating, thin beams.” *J. Acoust. Soc. Am.*, **114**(4):1785–1795, 2003.
- [ASL03] Y. Arntz, J. D. Seelig, H. P. Lang, J. Zhang, P. Hunziker, J. P. Ramseyer, E. Meyer, M. Hegner, and Ch. Gerber. “Label-free protein assay based on a nanomechanical cantilever array.” *Nanotechnology*, **14**:86, 2003.
- [Bat94] G. K. Batchelor. *An introduction to fluid dynamics*. Cambridge University Press, 1st paperback edition, 1994. p. 288.
- [BBR96] N. Blanc, J. Brugger, N. F. de Rooij, and U. Dürig. “Scanning force microscopy in the dynamic mode using microfabricated capacitive sensors.” *J. Vac. Sci. Technol. B*, **14**:901–905, 1996.
- [BDD99] G. Binnig, M. Despont, U. Drechsler, W. Häberle, M. Lutwyche, P. Vettiger, H. J. Mamin, B. W. Chui, and T. W. Kenny. “Ultrahigh-density atomic force microscopy data storage with erase capability.” *Appl. Phys. Lett.*, **76**:1329–1331, 1999.
- [BDL98] R. Berger, E. Delamarche, H. P. Lang, Ch. Gerber, J.K. Gimzewski, E. Meyer, and H.-J. Güntherodt. “Surface stress in the self-assembly of alkanethiols on gold probed by a force microscopy technique.” *Appl. Phys. A*, **66**:S55–S59, 1998.
- [Bel53] E. T. Bell. *Men of Mathematics*. Penguin Books, 1953. pp. 276–277.
- [Bir56] T. Birch. *History of the Royal Society*, **2**:475, 1756. London: A. Millar.
- [Bir57] T. Birch. *History of the Royal Society*, **4**:46, 1757. London: A. Millar.
- [BMB91] C. Burbaum, J. More, P. Bley, and W. Ehrfeld. “Fabrication of capacitive acceleration sensors by the LIGA technique.” *Sens. Act. A*, **25-27**:559–563, 1991.
- [Boy82] R. Boyle. *New experiments physico-mechanical, touching the air*. Miles Fleshner, London, 3rd edition, 1682. Expt. 27, p. 103.
- [BQG86] G. Binnig, C. F. Quate, and Ch. Gerber. “Atomic force microscope.” *Phys. Rev. Lett.*, **56**:930–933, 1986.

- [BSW00] A. Bietsch, M. A. Schneider, M. E. Welland, and B. Michel. “Electrical testing of gold nanostructures by conducting atomic force microscopy.” *J. Vac. Sci. Technol. B*, **18**:1160–1170, 2000.
- [BZH04] A. Bietsch, Jiayun Zhang, M. Hegner, H. P. Lang, and Ch. Gerber. “Rapid functionalization of cantilever array sensors by inkjet printing.” *Nanotechnol.*, **15**:873–880, 2004.
- [BZH05] N. Backmann, Ch. Zahnd, F. Huber, A. Bietsch, A. Plückthun, H. P. Lang, H.-J. Güntherodt, M. Hegner, and Ch. Gerber. “A label-free immunosensor array using single-chain antibody fragments.” *P. Natl. Acad. Sci.*, **102**:14587–14592, 2005.
- [CD48] M. R. Cohen and I. E. Drabkin. *A source book in Greek science*. Harvard University Press, 1948. pp. 286–310.
- [CGS02] A. Carvalho, M. Geissler, H. Schmid, B. Michel, and E. Delamarche. “Self-assembled monolayers of eicosanethiol on palladium and their use in microcontact printing.” *Langmuir*, **18**:2406–2412, 2002.
- [Chl87] E. F. F. Chladni. *Entdeckungen über die Theory des Klanges*. Breitkopf und Härtel, Leipzig, 1787.
- [Chl02] E. F. F. Chladni. *Die Akustik*. Breitkopf und Härtel, Leipzig, 1802.
- [Chl09] E. F. F. Chladni. *Traité d’Acoustique*. Courcier, Paris, 1809.
- [Chl17] E. F. F. Chladni. *Neue Beiträge zur Akustik*. Breitkopf und Härtel, Leipzig, 1817.
- [CMS00] J. W. M. Chon, P. Mulvaney, and J. E. Sader. “Experimental validation of theoretical models for the frequency response of atomic force microscope cantilever beams immersed in fluids.” *J. Appl. Phys.*, **87**:3978–3988, 2000.
- [Col93] J.-D. Colladon. *Souvenirs et mémoires: autobiographie de J.-Daniel Colladon*. Aubert-Schuchardt, Geneva, 1893.
- [CS27] J.-D. Colladon and J. K. F. Sturm. “Mémoire sur la compression des liquides et la vitesse du son dans l’eau.” *Ann. Chim. Phys.*, **36**:113, 225, 1827.
- [DAH03] Z. J. Davis, G. Abadal, B. Helbo, O. Hansen, F. Campabadal, F. Pérez-Murano, J. Esteve, E. Figueras, J. Verd, N. Barniol, and A. Boisen. “Monolithic integration of mass sensing nano-cantilevers with CMOS circuitry.” *Sens. Act. A*, **105**:311–319, 2003.
- [DMG94] E. Delamarche, B. Michel, Ch. Gerber, D. Anselmetti, H.-J. Güntherodt, H. Wolf, and H. Ringsdorf. “Real-space observation of nanoscale molecular domains in self-assembled monolayers.” *Langmuir*, **10**:2869–2871, 1994.
- [DSB97] U. Dürig, H. R. Steinauer, and N. Blanc. “Dynamic force microscopy by means of the phase-controlled oscillator method.” *J. Appl. Phys.*, **82**:3641–3651, 1997.
- [EKW90] A. Eychmüller, L. Katsikas, and H. Weller. “Photochemistry of semiconductor colloids. 35. Size separation of colloidal CdS by gel electrophoresis.” *Langmuir*, **6**:1605–1608, 1990.

- [Far31] M. Faraday. "On a peculiar class of acoustical figures; and on certain forms assumed by groups of particles upon vibrating elastic surfaces." *Philosophical Transactions of the Royal Society of London*, pp. 299–318, 1831.
- [FBL00] J. Fritz, M. K. Baller, H. P. Lang, H. Rothuizen, P. Vettiger, E. Meyer, H.-J. Güntherodt, Ch. Gerber, and J. K. Gimzewski. "Translating Biomolecular Recognition into Nanomechanics." *Science*, **288**:316–318, 2000.
- [FEU95] T. L. Freeman, S. D. Evans, and A. Ulman. "XPS studies of self-assembled multilayer films." *Langmuir*, **11**:4411–4417, 1995.
- [FKK05] T. Fukuma, M. Kimura, K. Kobayashi, K. Matsushige, and H. Yamada. "Development of low noise cantilever deflection sensor for multienvironment frequency-modulation atomic force microscopy." *Rev. Sci. Instrum.*, **76**:053704, 2005.
- [FWK89] Ch.-H. Fischer, H. Weller, L. Katsikas, and A. Henglein. "Photochemistry of colloidal semiconductors. 30. HPLC investigation of small CdS particles." *Langmuir*, **5**:429–432, 1989.
- [FYC02] F.-R. F. Fan, J. Yang, L. Cai, D. W. Price, S. M. Dirk, D. V. Kosynkin, Y. Yao, A. M. Rawlett, J. M. Tour, and A. J. Bard. "Charge Transport through Self-Assembled Monolayers of Compounds of Interest in Molecular Electronics." *J. Am. Chem. Soc.*, **124**:5550–5560, 2002.
- [FYC04] F.-R. F. Fan, Y. Yao, L. Cai, L. Cheng, J. M. Tour, and A. J. Bard. "Structure-Dependent Charge Transport and Storage in Self-Assembled Monolayers of Compounds of Interest in Molecular Electronics: Effects of Tip Material, Headgroup, and Surface Concentration." *J. Am. Chem. Soc.*, **126**:4035–4042, 2004.
- [GGM94] J. K. Gimzewski, Ch. Gerber, E. Meyer, and R. R. Schlittler. "Observation of a chemical reaction using a micromechanical sensor." *Chem. Phys. Lett.*, **217**:589–594, 1994.
- [GM98] N. G. Green and H. Morgan. "Separation of submicrometre particles using a combination of dielectrophoretic and electrohydrodynamic forces." *J. Phys. D*, **31**:L25–L30, 1998.
- [Heg00] M. Hegner. "DNA handles for single molecule experiments." *Single Mol.*, **1**:139–144, 2000.
- [Her96] G. T. Hermanson. *Bioconjugate techniques*. Academic, San Diego, 1996.
- [Hie11] K. Hiemenz. *Die Grenzschicht an einem in den gleichförmigen Flüssigkeitsstrom eingetauchten geraden Kreiszyylinder*. PhD thesis, Göttingen, 1911. Or: *Dingler's Polytech. J.*, **326**:311.
- [HKK04] S. Hur, D. Khang, C. Kocabas, and J. Rogers. "Nanotransfer printing by use of non-covalent surface forces: Applications to thin-film transistors that use single-walled carbon nanotube networks and semiconducting polymers." *Appl. Phys. Lett.*, **85**:5730–5732, 2004.

- [HMG88] H. Heinzelmann, E. Meyer, P. Grütter, H.-R. Hidber, L. Rosenthaler, and H.-J. Güntherodt. “Atomic force microscopy: General aspects and application to insulators.” *J. Vac. Sci Technol. A*, **6**:275–278, 1988.
- [HR03] J. R. Heath and M. A. Ratner. “Molecular electronics.” *Physics Today*, **56**:43–49, 2003.
- [HR04] D. A. Huerta and J. C. Ruiz-Suárez. “Vibration-Induced Granular Segregation: A Phenomenon Driven by Three Mechanisms.” *Phys. Rev. Lett.*, **92**:114301, 2004.
- [HW01] A. Hatzor and P. S. Weiss. “Molecular Rulers for Scaling Down Nanostructures.” *Science*, **291**:1019–1020, 2001.
- [IAM93] S. Inaba, K. Akaishi, T. Mori, and K. Hane. “Analysis of the resonance characteristics of a cantilever vibrated photothermally in a liquid.” *J. Appl. Phys.*, **73**:2654–2658, 1993.
- [KBB03] K. Keren, R. S. Berman, E. Buchstab, U. Sivan, and E. Braun. “DNA-Templated Carbon Nanotube Field-Effect Transistor.” *Science*, **302**:1380–1382, 2003.
- [KMD05] T. Kraus, L. Malaquin, E. Delamarche, H. Schmid, N. D. Spencer, and H. Wolf. “Closing the Gap Between Self-Assembly and Microsystems Using Self-Assembly, Transfer, and Integration of Particles.” *Adv. Mater.*, **17**:2438–2442, 2005.
- [LB02] H. Li and R. Bashir. “Dielectrophoretic separation and manipulation of live and heat-treated cells of *Listeria* on microfabricated devices with interdigitated electrodes.” *Sens. Act. B*, **86**:215–221, 2002.
- [LB03] S. W. Lee and R. Bashir. “Dielectrophoresis and electrohydrodynamics-mediated fluidic assembly of silicon resistors.” *Appl. Phys. Lett.*, **83**:3833–3835, 2003.
- [LBC04] M. D. LaHaye, O. Buu, B. Camarota, and K. C. Schwab. “Approaching the Quantum Limit of a Nanomechanical Resonator.” *Science*, **304**:74–77, 2004.
- [Len51] L. M. A. Lenihan. “Mersenne and Gassendi. An early chapter in the history of sound.” *Acustica*, **2**:96–99, 1951.
- [Lid94] D. R. Lide, editor. *CRC Handbook of chemistry and physics*. CRC Press, Boca Raton, FL, 75th edition, 1994.
- [Lin66] R. B. Lindsay. “The story of acoustics.” *J. Acoust. Soc. Am.*, **39**:629–644, 1966.
- [Lin73] R. B. Lindsay, editor. *Acoustics: historical and philosophical development*. Dowden, Hutchinson & Ross, Stroudsburg, PA, 1973.
- [LNB05] R. J. Linderman, O. Nilsen, and V. M. Bright. “Electromechanical and fluidic evaluation of the resonant microfan gas pump and aerosol collector.” *Sens. Act. A*, **118**:162–170, 2005.
- [LPM02] K.-B. Lee, S.-J. Park, C. A. Mirkin, J. C. Smith, and M. Mrksich. “Protein Nanoarrays Generated By Dip-Pen Nanolithography.” *Science*, **295**:1702–1705, 2002.

- [LWB04] D. W. Lee, A. Wetzel, R. Bennewitz, E. Meyer, M. Despont, P. Vettiger, and Ch. Gerber. “Switchable cantilever for a time-of-flight scanning force microscope.” *Appl. Phys. Lett.*, **84**:1558–1560, 2004.
- [MA88] G. Meyer and N. M. Amer. “Novel optical approach to atomic force microscopy.” *Appl. Phys. Lett.*, **53**:1045–1047, 1988.
- [Mac38] E. MacCurdy. *Notebooks of Leonardo da Vinci*. Jonathan Cape, London, 1938. p. 559 (*Concerning the local movement of flexible dry things such as dust and the like*).
- [Med] Medical University of Carolina, http://bcr.musc.edu/manuals/AUTODOCK_DOC/AD3.a.0UserGuide.html. *Autodock manual*. Chapter 8: Van der Waals Potential Energy.
- [Mel88] F. Melde. *Chladni’s Leben und Wirken*. N. G. Elwert’sche Verlagsbuchhandlung, Marburg, 2nd edition, 1888.
- [MHS04] H. Ma, J. Hyun, P. Stiller, and A. Chilkoti. ““Non-fouling” oligo(ethylene glycol)-functionalized polymer brushes synthesized by surface-initiated atom transfer radical polymerization.” *Adv. Mater.*, **16**:338–341, 2004.
- [MMA96] S. R. Manalis, S. C. Minne, A. Atalar, and C. F. Quate. “Interdigital cantilevers for atomic force microscopy.” *Appl. Phys. Lett.*, **69**:3944–3946, 1996.
- [MNB93] C. B. Murray, D. J. Norris, and M. G. Bawendi. “Synthesis and characterization of nearly monodisperse CdE (E = S, Se, Te) semiconductor nanocrystallites.” *J. Am. Chem. Soc.*, **115**:8706–8715, 1993.
- [Nyb98] W. L. Nyborg. “Acoustic Streaming.” In M. F. Hamilton and D. T. Blackstock, editors, *Nonlinear Acoustics*, chapter 7, pp. 207–231. Academic, San Diego, 1998.
- [PBA87] M. D. Porter, T. B. Bright, D. L. Allara, and C. E. D. Chidsey. “Spontaneously organized molecular assemblies. 4. Structural characterization of n-alkyl thiol monolayers on gold by optical ellipsometry, infrared spectroscopy, and electrochemistry.” *J. Am. Chem. Soc.*, **109**:3559–3568, 1987.
- [Ray84] Lord Rayleigh. “On the circulations of air observed in Kundt’s tubes and on some allied acoustical problems.” *Phil. Trans. Roy. Soc. Lond.*, **175**:1–21, 1884.
- [RBM04] D. Rugar, R. Budakian, H. J. Mamin, and B. W. Chui. “Single spin detection by magnetic resonance force microscopy.” *Nature*, **430**:329–332, 2004.
- [RER05] A. Ros, R. Eichhorn, J. Regtmeier, T. Duong, P. Reimann, and D. Anselmetti. “Absolute negative particle mobility.” *Nature*, **436**:928, 2005.
- [Ril01] N. Riley. “Steady Streaming.” *Annu. Rev. Fluid. Mech.*, **33**:43–65, 2001.
- [RMG89] D. Rugar, H. J. Mamin, and P. Guethner. “Improved fiber-optic interferometer for atomic force microscopy.” *Appl. Phys. Lett.*, **55**:2588–2590, 1989.

- [RSP87] A. Rosato, K. J. Strandburg, F. Prinz, and R. H. Swendsen. “Why the Brazil nuts are on top: size segregation of particulate matter by shaking.” *Phys. Rev. Lett.*, **58**:1038–1040, 1987.
- [RSW98] M. A. Rampi, O. J. A. Schueller, and G. M. Whitesides. “Alkanethiol self-assembled monolayers as the dielectric of capacitors with nanoscale thickness.” *Appl. Phys. Lett.*, **72**:1781–1783, 1998.
- [RYS92] D. Rugar, C. S. Yannoni, and J. A. Sidles. “Mechanical detection of magnetic resonance.” *Nature*, **360**:563–566, 1992.
- [SA89] C. Schönenberger and S. F. Alvarado. “A differential interferometer for force microscopy.” *Rev. Sci. Instrum.*, **60**:3131–3134, 1989.
- [Sad05] J. E. Sader. “Dynamics of microcantilevers in fluids.” In *Cantilever Sensors Idea Exchange*. NCCR Nanoscale Science, Basel, Switzerland, 2005.
- [SBF03] C. A. Savran, T. P. Burg, J. Fritz, and S. R. Manalis. “Microfabricated mechanical biosensor with inherently differential readout.” *Appl. Phys. Lett.*, **83**:1659–1661, 2003.
- [SDA02] A. D. Stroock, S. K. W. Dertinger, A. Ajdari, and I. Mezić. “Chaotic mixer for microchannels.” *Science*, **295**:647–651, 2002.
- [Sem05] J. M. Seminario. “Approaching reality.” *Nat. Mater.*, **4**:111–112, 2005.
- [SG00] H. Schlichting and K. Gersten. *Boundary layer theory*. Springer, 8th edition, 2000.
- [Sim63] J. G. Simmons. “Generalized formula for the electric tunnel effect between similar electrodes separated by a thin insulating film.” *J. Appl. Phys.*, **34**:1793–1803, 1963.
- [SKF00] H. Sirringhaus, T. Kawase, R. H. Friend, T. Shimoda, M. Inbasekaran, W. Wu, and E. P. Woo. “High-Resolution Inkjet Printing of All-Polymer Transistor Circuits.” *Science*, **290**:2123–2126, 2000.
- [SL01] A. Sathaye and A. Lal. “An acoustic vortex generator for microfluidic particle entrapment.” In *2001 IEEE Ultrasonics Symposium*, pp. 641–644, 2001.
- [SLM95] J. E. Sader, I. Larson, P. Mulvaney, and L. R. White. “Method for the calibration of atomic force microscope cantilevers.” *Rev. Sci. Instrum.*, **66**:3789–3798, 1995.
- [Tel81] D. P. Telionis. *Unsteady viscous flows*. Springer-Verlag, New York, 1981.
- [TP89] C. H. Ting and M. Paunovic. “Selective electroless metal-deposition for integrated-circuit fabrication.” *J. Electrochem. Soc.*, **136**:456–462, 1989.
- [TYB91] M. Tortonese, H. Yamada, R. C. Barrett, and C. F. Quate. “Atomic force microscopy using a piezoresistive cantilever.” In *TRANSDUCERS '91: International Conference on Solid State Sensors and Actuators*, pp. 448–451, 24–27 Jun 1991.
- [VGC93] T. G. Vargo, J. A. Gardella, J. M. Calvert, and M. S. Chen. “Adhesive electroless metallization of fluoropolymeric substrates.” *Science*, **262**:1711–1715, 1993.

- [WDH96] S. Weigert, M. Dreier, and M. Hegner. "Frequency shifts of cantilevers vibrating in various media." *Appl. Phys. Lett.*, **69**:2834–2836, 1996.
- [WHR02] D. J. Wold, R. Haag, M. A. Rampi, and C. D. Frisbie. "Distance Dependence of Electron Tunneling through Self-Assembled Monolayers Measured by Conducting Probe Atomic Force Microscopy: Unsaturated versus Saturated Molecular Junctions." *J. Phys. Chem. B*, **106**:2813–2816, 2002.
- [wik] Wikipedia, *Hydrogen bond*, website: http://en.wikipedia.org/wiki/Hydrogen_bond.
- [win05] "Surface Modifications from Solution." Course Reader of Industrial Chemistry, Zürcher Hochschule Winterthur, November 2005.
- [WLR05] W. Wang, T. Lee, and M. A. Reed. "Electronic Transport in Molecular Self-Assembled Monolayer Devices." *Proc. IEEE*, **93**:1815–1824, 2005.
- [WN06] M. S. Wilson and W. Nie. "Electrochemical Multianalyte Immunoassays Using an Array-Based Sensor." *Anal. Chem.*, **78**:2507–2513, 2006.
- [ZBC02] M. Zhang, D. Bullen, S.-W. Chung, S. Hong, K. S. Ryu, Z. Fan, C. A. Mirkin, and C. Liu. "A MEMS nanoplotter with high-density parallel dip-pen nanolithography probe arrays." *Nanotechnology*, **13**:212–217, 2002.

Curriculum Vitae

Name : Marko Dorrestijn
Date of Birth : October 1, 1973
Place of Birth : Griesbach, Germany
Nationality : Dutch

Education

- 2002 – 2006 Ph.D. research at IBM Research GmbH, Switzerland
in ‘Physics of Nanoscale Systems’ group of Dr. R. Allenspach
and at Institute of Physics, University of Basel, Switzerland
in ‘Biophysics’ group of Dr. M. Hegner
Thesis advisors: Prof. Dr. Christoph Gerber and Prof. Dr. Ernst Meyer
Title: *Nanomechanical sensing in liquid*
- 2005 IBM Micro MBA
IBM Research / Stern School of Business / Columbia Business School
Five-month program focusing on corporate finance and marketing
- 2000 – 2002 M.Sc. in Applied Physics at Delft University of Technology
Grade average (10-pt. scale): 8; 9 in practical courses
M.Sc. research in ‘Molecular Biophysics’ group of Prof. Dr. C. Dekker
Title: *Assembly of double-stranded DNA molecules embedded in
alkanethiolate self-assembled monolayers on gold*
- 1995 – 2000 B.Sc. in Applied Physics at Delft University of Technology
Thesis research in ‘Analytical Biotechnology’ group of Prof. Dr. Th. Schalkhammer
Title: *Towards single-molecule detection with nanocluster-based biosensors*
- 1993 – 1995 Propaedeuse in Mechanical Engineering at Delft University of Technology
1986 – 1993 Gymnasium Atheneum College Hageveld, Heemstede, The Netherlands

Honors

- 2005 IBM Innovation Award
2001 Dutch Physics Olympiade: 1st place
2000 Bachelor’s thesis: grade 10 (10-pt. scale)

Publications

Patents

M. Dorrestijn, A. Bietsch, Ch. Gerber, E. Meyer, "Displacement sensor comprising a squeezable insulator", pending patent application UK 0512657.8 (2005).

Journal publications

M. Dorrestijn, A. Bietsch, H. P. Lang, E. Meyer, Ch. Gerber, "A tunneling displacement sensor based on a squeezable molecular bilayer", *Nanotechnology* 17 (2005) 2242–2245.

M. Dorrestijn, A. Bietsch, T. Açikalin, A. Raman, M. Hegner, E. Meyer, Ch. Gerber, "Chladni Figures Revisited based on Nanomechanics", submitted (2006).

M. Dorrestijn, A. Raman, E. Meyer, Ch. Gerber, "The physics of boundary streaming", in preparation (2006).

Course readers

M. Dorrestijn, "Negotiating and Telephoning", course reader for Delft University of Technology, May 1997.

M.Sc. thesis

M. Dorrestijn, "Assembly of double-stranded DNA molecules embedded in alkanethiolate self-assembled monolayers on gold", Master's Thesis, Dpt. of Applied Physics, Delft University of Technology, The Netherlands, May 8, 2002.

B.Sc. thesis

M. Dorrestijn, "Towards single-molecule detection with nanocluster-based biosensors", Bachelor's Thesis, Kluyver Laboratory of Biotechnology, Delft University of Technology, The Netherlands, September 26, 2000.